DISCLAIMER

Lawrence Livermore National Laboratory

LLNL-TR-2007989

Simulation of Physics-Based 0-10Hz Strong Motion Using High Performance Computing Supporting Refinements to Regional Ground Motion Models for the

A Aguiar Moya, A Pitarka, V Graizer, A Rodgers

September 2025

Disclaimer

This work performed under the auspices of the U.S. Department of Energy by Lawrence Livermore National Laboratory under Contract DE-AC52-07NA27344.

Simulation of Physics-Based 0-10Hz Strong Motion Using High Performance Computing Supporting Refinements to Regional Ground Motion Models for the Central Eastern US

Arben Pitarka[1], Vladimir Graizer[2], Ana Aguiar[1], and Arthur Rodgers[1]

[1]Lawrence Livermore National Laboratory, Livermore CA

[2]U.S. Nuclear Regulatory Commission

This work was performed under the auspices of the U.S. Department of Energy by Lawrence Livermore National Laboratory under Contract DE-AC52-07NA27344

1.0 EXECUTIVE SUMMARY

In collaboration with the U.S. Nuclear Regulatory Commission (NRC) the LLNL has developed a computationally efficient simulation platform designed to perform physics-based ground motion simulations for crustal earthquakes in the Stable Continental Regions of Central and Eastern US (CEUS), using high-performance computing. The main objective of the earthquake simulations was to use synthetic ground motion to provide constrains to refinements of existing ergodic Ground Motion Models (GMMs), for large magnitude earthquakes and near-fault distances, for which these models are less reliable. Physics-based broadband (0-10Hz) ground motion simulations were used to estimate the near-fault ground motion amplitudes and within event and between-event variabilities associated with fault rupture characteristics.

In our simulations we used a 3D regional velocity model that was based on Saikia's 1D velocity model (1994). In simulations performed during the first stage of this project the Saikia's velocity model demonstrated better performance in modelling high frequency regional wave propagation for the CEUS region recorded during the *Mw*5.0 November 7, 2016, Cushing Oklahoma (Taylor et al., 2017), and *Mw*5.8 September 3, 2016, Pawnee Oklahoma earthquakes. The proposed regional 3D model includes random perturbations to the 1D background model using the stochastic scheme of Pitarka and Mellors (2021). In addition, validation analysis of the rupture generator and regional wave propagation models, using comparisons with different GMMs for *Mw*6.5 and *Mw*7.0 scenario earthquakes in the CEUS region resulted in a very good match between the simulated and empirical ground motion models.

For the purposes of seismic hazard assessment at the existing and planned nuclear power plants, NRC is interested in studies aimed at improving the current ground motion models (GMM) for both Stable Continental Regions (SCR) in the Central and Eastern US and Active Crustal Regions (ACR) in the Western US. Due to lack of recorded data, these improvements require synthetic data for short fault distances and large magnitude earthquakes for which the existing recorded data is not enough to uniquely constrain the GMMs. The need for simulations and strong motion data is especially critical for the CEUS region where we do not have recorded data from potentially large damaging earthquakes with moment magnitudes 6.0 and higher. In this the project, we focused on 10Hz simulations of Mw7.0 scenario earthquakes with strike slip and thrust faulting mechanisms. We used more than 50 *Mw*7.0 earthquake rupture scenarios to investigate the ground motion uncertainty due to unknown earthquake rupture parameters, in particular, the slip distribution, rupture velocity, and faulting mechanism, and their implication on ground motion amplification due to forward rupture directivity effects.

Our analysis of simulated ground motion for *Mw*6.5 and *Mw*7 earthquakes for CEUS demonstrate that the LLNL physics based deterministic approach produces ground motion compatible with the GMMs and recorded ones for small and moderate earthquakes. Comparisons with GMMs for a *Mw*7.0 earthquake in the CEUS region resulted in a good match between the simulated and empirical ground motion models for spectral accelerations (SA) at periods > 0.2s. Our investigation of within-event and between-event ground motion variabilities for *Mw*7.0 scenario earthquakes on a strike-slip fault, suggest that, similarly to Mw6.5 earthquakes, they are strongly related to spatial

slip and slip rate variations, average rupture velocity, and rupture area. We found that the ground motion variability observed at near-fault distances also persists at longer distances. The simulated ground motion for both *Mw*6.5 and *Mw*7.0 earthquakes tends to fully saturate at short distances for all periods. The simulations suggest that the near fault ground motion saturation is not only magnitude dependent but also period dependent. The near-fault saturation can be explained by the combined effects of wave scattering attenuation along the fault and local source radiation pattern. Our analysis of the effects of rupture initiation location suggests that the peak ground motion (PGV) and spectral acceleration (SA) can vary substantially along the fault as a direct consequence of rupture kinematics, including rupture directivity. Such effects are stronger at periods longer than 1s.

Our sensitivity analysis suggests that the rupture parameters with the strongest contribution to simulated ground motion uncertainty are the rupture velocity, location of large slip areas, and rupture area. The large set of synthetic ground motion generated during this project can be used to constrain the existing GMMs, especially for large magnitudes and short distances.

In an attempt for estimating the ground motion amplitude, and fault location, during the Mw7.0, 1887 Charleston earthquake, we applied our simulation technique to perform a suite of ground motion simulations in which we used several rupture scenarios with the fault geometry constrained by geological and geophysical data, and current local seismicity. The comparison of the simulated ground motion amplification patterns obtained for different rupture scenarios, and the free surface soil damage observed soon after the earthquake, favors the location of the fault, rupture area and faulting mechanism proposed by Chapman and Beale (2020). Our simulations also suggest that the forward rupture directivity effects might have played a role in the observed surface manifestation of ground motion intensity patterns.

Interim findings of the project were presented at the international meeting Future Directions: Physics-based ground motion modeling in Vancouver, Canada in October 2013. The main findings from this project were presented at the DOE-NRC NPH Workshop October 29-30, 2024 (Pitarka et al., 2024) and at a project report meeting at the NRC HQ, Rockville **MD, May 27, 2025.**

1.0 INTRODUCTION

This collaborative study between the LLNL and NRC aims at testing a high-performance computing simulation platform for ground motion simulations that will be used to develop physical constrains needed to guide improvements of Ground Motion Models (GMMs) for crustal earthquakes at short distances and large magnitudes. The Seismology Group at the LLNL has developed a physics-based earthquake rupture model generator and computationally efficient methods for earthquake ground motion simulations. The LLNL simulation technique allows for regional-scale wave propagation modelling in highly heterogenous media with realistic surface topography enabled by the curvilinear mesh finite-difference formulation with grid refinements adopted by the SW4. SW4 is a wave

propagation modelling computer program developed at the LLNL that can be obtained through the Computational Infrastructure for Geodynamics website specialized in validated computer programs for geophysics (https://geodynamics.org/cig/software/sw4/). The Graves and Pitarka (GP) (Graves and Pitarka, 2016) physics-based earthquake rupture generator adopted in the platform has been validated against recorded ground motions from recent earthquakes in California and Japan (e.g., Pitarka et al.,2022; Pitarka e al, 2017; Rodgers et al., 2019,2020). It allows for deterministic ground motion simulations in the frequency range 0–10 Hz which is critical in the evaluation of NPP structures.

The main objective of the project is to provide technical capabilities for producing physics-based ground motion that can be used to constrain the GMMs for Stable Continental Regions (SCR) and Active Crustal Regions (ACR) at short distances and large magnitudes. The first phase of the project was mainly focused on validating the 3D regional model, used in simulations, by comparing recorded and synthetic ground motion for moderate events, and analysing the performance of the simulation platform in ground motion simulations of Mw6.5 earthquakes on a strike slip fault by comparing the simulated ground motion with GMMs. The successful completion of the first phase opened the way to performing simulations of Mw7.0 earthquakes and extending the maximum modelled frequency to 10Hz. The synthetics were used to analyse the ground motion saturation used in constraining the GMMs for short distances. Similar to the analysis performed during the first phase, through multiple realisations of the earthquake rupture the scenario-based simulations were designed to investigate the ground motion variability due to different kinematic rupture model parameters, including slip distribution, peak slip rate, rupture velocity, rupture area and hypocenter location. The unknown range of these parameters is the source of uncertainties in probabilistic and deterministic seismic hazard assessment. Special attention was placed on the investigation of rupture velocity and faulting mechanism effects on near-fault ground motion.

2.0 GROUND MOTION SIMULATION OF Mw7.0 SCENARIO EARTHQUAKES ON A STRIKE SLIP VERTICAL FAULT

The simulations of Mw7.0 scenario earthquakes were performed in the frequency range 0-10 Hz using a 3D reginal model, based on Saikia's 1D reginal velocity model (Saikia, 1994), covering an area of 90km x 110km, with depth extending to 40 km, with modest surface topography from western North Carolina (shown in Figure 1). The performance of Saika's 1D model and that of Herrman (1995), shown in Figure 2, was thoroughly investigated during the first phase of this project where we compared recorded and simulated ground motion for two CEUS earthquakes. Saikia's 1D model provided a better goodness of fit, especially at high frequencies.

In all simulations we used a 3D regional velocity model with a minimum grid spacing of 12.5 m that ensures a numerical accuracy up to the target frequency of 10Hz for a min Vs = 1000m/s. The ground motion time histories are computed on a dense grid of stations with a 2 km grid spacing. The stations spacing is reduced to 1km at fault distances smaller than 5 km. The 3D velocity model is designed to capture wave propagation effects on hard rock, including overall low attenuation that is typical for CEUS regions. The high frequency wave scattering effect is modelled by including small-scale structural variations in the velocity model. The small-scale variations are introduced by correlated random perturbations of the velocity, generated with the von Karman model following Pitarka and Mellors (2021). Figure 3 illustrates the small-scale variation in shallow sedimentary layers generated with our stochastic modelling scheme. The parameters of stochastic velocity perturbations are applied in the depth range 0-7km. Their depth dependent variation is shown in Table 1.

Table 1*. Stochastic Velocity Model Parameters used in the von Karman's stochastic model*

Depth (m)	Lx: horizontal correlation length (m)	Lz: vertical correlation length (m)	sigma	Hurst Number
0-2000	1000	250	0.08	0.1
2-5000	2000	500	0.05	0.4

2.1 Kinematic Rupture Models

The kinematic rupture models representing different rupture scenarios were generated with the GP method (Graves and Pitarka, 2016). The GP rupture model is derived from dynamic rupture modelling and is constrained by empirical relationships between the slip and other kinematic rupture parameters such as peak slip rate, rise time, and rupture velocity. The rupture heterogeneity is achieved by correlated random perturbations at different scale lengths. The resulting rupture model incorporates depth-dependent multi-scale spatial variations of slip, slip rate, local faulting mechanism, and rupture velocity, that allow for producing realistic near-fault ground motion on a broad frequency range (Graves and Pitarka,2016; Pitarka et al., 2022). For example, the longer rise time at shallow depths and shorter rise time at greater depths, are designed to represent the depth-dependent frequency content of the seismic energy generated by the fault rupture. We used Somerville at al formula (2021) to calculate the average rise time Tr and rupture area A, developed for Cratonic (stable part of a continent's crust) regions:

$$Tr = 2.1 * 1.0e\text{-}0.9 * \exp^{(\log(Mo/3))}]$$

$$\text{Log}_{10}A = Mw - 4.25$$

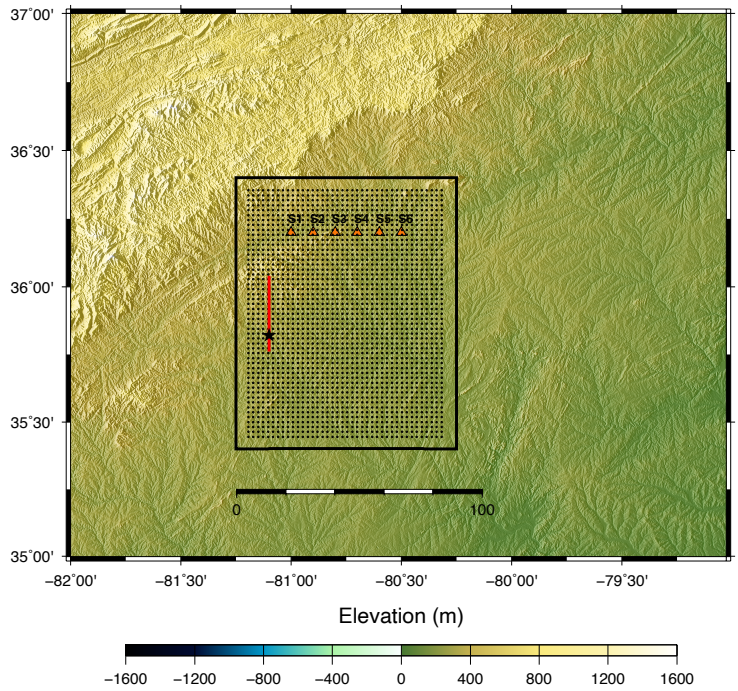

Figure 1. Map of the study area. The black rectangle indicates the model location, and the red line indicates the vertical fault trace used in the simulations of Mw7.0 earthquakes on a vertical strike-slip fault. The star indicates the rupture initiation location for the base rupture model; the black dots indicate the grid of stations used in the simulated ground motion analysis.

In our rupture models we used a planar fault with a length of 50 km, and width of 15 km. Except for rupture scenarios used in analysis of ground motion sensitivity to rupture velocity, the average rupture velocity is set to 82% of the local shear wave velocity, in accordance with observed rupture velocity values found for shallow crustal earthquakes on mature faults. Note that the GP assigns small-scale rupture variations that correlate with the local slip, the rupture speed increases in areas where slip is higher and decreases where the slip is lower. The depth to the top of the fault was set to 0.2 km and the dip angle is 90 degrees. The earthquake focal mechanism is assumed to be predominantly of strike-slip type. The average rake angle is set to 0 degree with spatially correlated random perturbations, computed following the GP method.

In this project we generated 45 rupture scenarios to capture the inherited ground motion variability due to several rupture characteristics such as slip pattern, rupture velocity, hypocenter location and faulting type. As shown in Table 2 the rupture scenarios were divided in six groups. Within each group we vary a single rupture parameter while keeping the other rupture parameters fixed. By varying one by one the source parameters, we

were able to separate their individual influence on simulated ground motion. Figure 4 illustrates kinematic rupture models with different slip distributions. As part of the parametrical study, in our analysis we also considered several rupture scenarios with a large slip patch located near the free surface.

3.0 SIMULATED GROUND MOTION VALIDATIONS AGAINST GMMs FOR THE CENTRAL-EASTERN U.S.

One of the main focused areas of this study was testing the quality of simulations by comparing them with Ground Motion Models (GMMs). The similarity of our simulations to GMMs builds confidence in our modelling capability. In the comparisons we used two available GMMs for Central-Eastern US:

1. NGA-East (Goulet et al, 2018): This model includes 17 GMMs defined for 24 ground-motion intensity measures, applicable to CENA in the moment magnitude range of 4.0 to 8.2 and covering distances up to 1500 km.
2. G-16v2 model (Graizer, 2017): This model is based on the NGA-East horizontal peak ground acceleration database and 5% damped pseudo spectral acceleration RotD50 component. The model is applicable for the stable continental regions and covers the following range: 4:0 ≤ Mw ≤8.5, 0 ≤ *Rrup* ≤ 1000 km, 300 ≤ VS_{30} ≤ 2800 m/s, and frequencies 0.1 ≤ *f* ≤ 100 Hz.

The NGA-East model, obtained for a VS_{30} = 2800 m/s, was corrected for VS_{30} =1000 m/s, using Graizer's GMM (Graizer, 2017) site factor model.

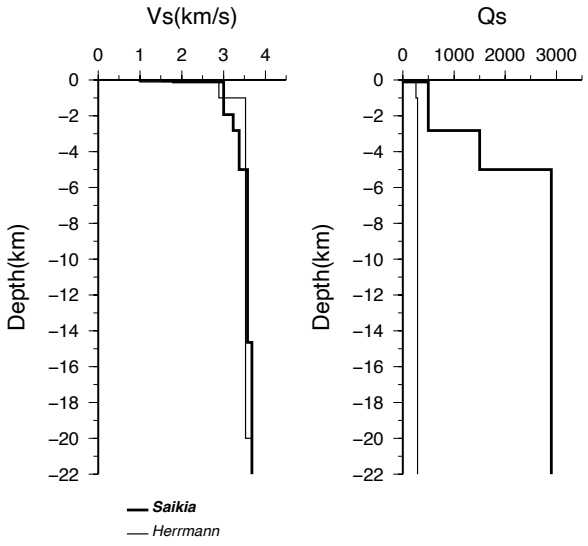

Figure 2. 1D velocity (left panel) and attenuation (right panel) models considered in building a reginal 3D model for the CEUS. Thick line corresponds to the model proposed by Saikia (1994) and thin line corresponds to the model proposed by Herrmann (1995).

Shallow Geology

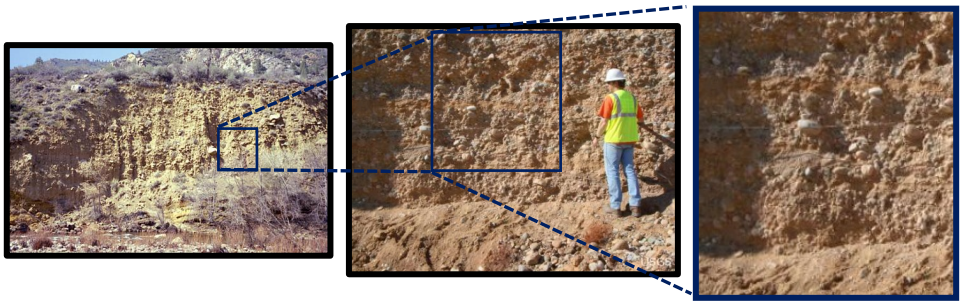

a) Stochastic model of heterogenous stratigraphy

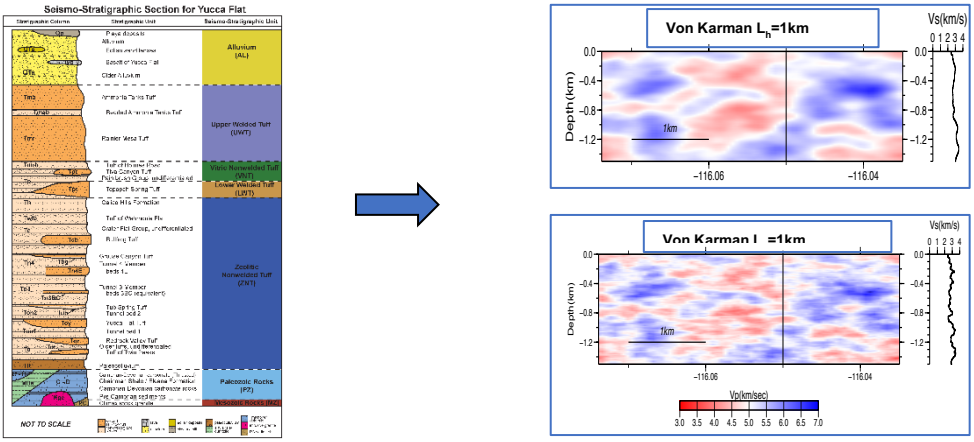

Figure 3. a) Pictures illustrating multiscale variability of the near-surface geology. b) Stochastic velocity models with correlated random perturbations.

Table 2. *Mw7.0 Rupture Scenarios Used in the Simulations*

Group	***Varied Rupture Parameter***	***Number of scenarios***
Group 1	Slip distribution	10
Group 2	Rupture velocity (60%,70%, 80% of Vs)	10
Group 3	Peak slip rate (+/-20%)	10
Group 4	Rupture with slip patches	6

Group 5	Hypocenter location (varies along strike)	5
Group 6	Thrust mechanism	4

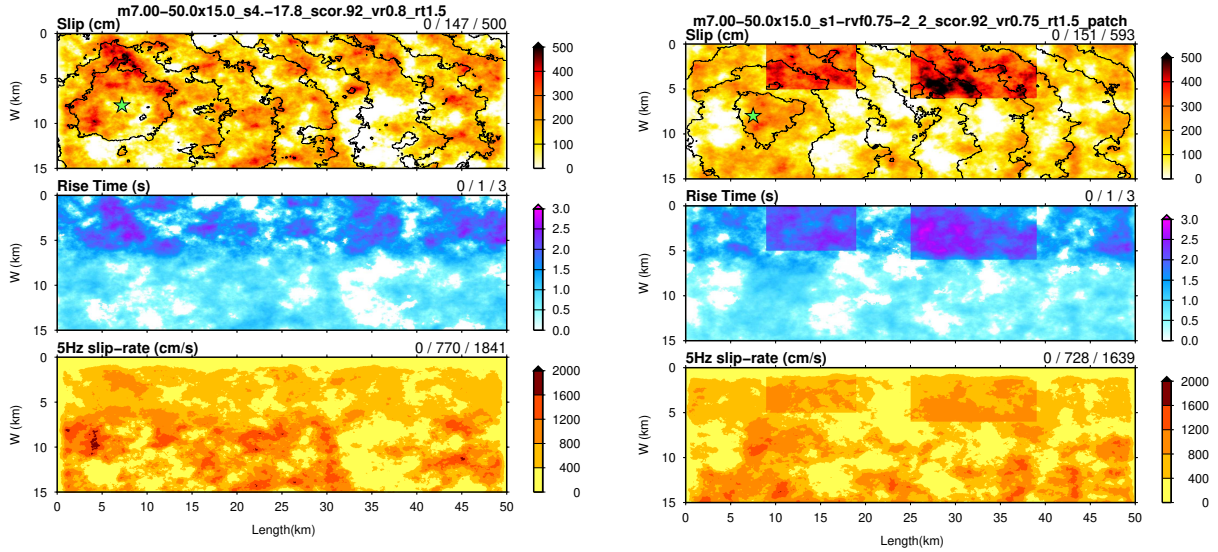

Figure 4. Kinematic rupture models generated with the Graves and Pitarka methodology (Pitarka et al., 2022) used in ground motion simulations of Mw7.0 strike slip earthquakes. Left panel: rupture model with a fully stochastic slip distribution. Right panel: rupture model with a hybrid slip that includes two large slip patches. In each rupture model, the top panel shows the slip distribution and the rupture time indicated by contour lines, the middle panel shows the rise time distribution, and the bottom panel shows the peak slip rate distribution flow-pass filtered at 5Hz. The hypocenters are indicated by the green star. The numbers shown on top of each panel indicate the minimum, average, and maximum values of slip, rise time and peak slip rate, respectively.

Table 3. 1D Regional Velocity Model Used in Generating a 3D Velocity Model for CEUS

Depth (m)	**Vp (m/s)**	**Vs(m/s)**	**Density (g/cm3)**	**Qp**	**Qs**
30.7	1730	1000	2030	100	50
44.7	2683	1551	2140	100	50
100.0	3119	1803	2276	100	50

1933.0	5190	3000	2611	1000	500
2828	5577	3224	2665	1000	500
5000	5828	3369	2700	3000	1500
14650	6180	3570	2724	5800	2900
25650	6360	3680	2781	5800	2900
33650	7120	4120	3066	5800	2900
36000	7260	4200	3094	5800	2900

Figure 5 illustrates the performance of the simulations for the four rupture scenarios with different slip distribution, including one with large slip patches. In this figure we show the comparison of the RotD50 SA for the NGA-East and G-16v2 (Graizer, 2017) GMMs with RotD50 SA computed for the spectral periods 0.5s, 1s, 2s, and 5s. The simulations performed remarkably well. The synthetic and empirical motions compare very well at all periods and distances. The slight discrepancy observed at the 5s period, at which the empirical ground motion is slightly higher than the one produced with two of the four scenarios, indicates that as expected, the slip distribution in our rupture models can also contribute to the between-event long period ground motion variability.

The simulated ground motion is fully saturated at near-fault distances (<10km). This important result is consistent with the saturation constraint adopted in the Grazer's GMM and some other models proposed for this region, at all periods, except for the 5s response for which the simulations suggest a slight oversaturation. We will discuss this, as well as its sensitivity to the style of faulting in a subsequent section. These results demonstrate the advantages of using simulated near-fault ground motions to supplement the limited available database of recordings for large earthquakes at small distances.

We extended our comparison to ground motions computed for all rupture scenarios, except for the models with a thrust faulting mechanism. The analysis of the thrust faulting scenarios is shown in a subsequent section of the report. Figure 6 illustrates the performance of the simulations. In this figure we show the comparison of the RotD50 SA computed for the spectral periods 0.5s, 0.75s 1s, 2s, 3s, 5s, 7.5s, and 10s. Overall, the simulated ground motion compares relatively well at periods shorter than 2s. At longer periods and at distances smaller than 20 km our simulated median ground motion is slightly lower than the median value estimated by both GMMs. Some of the rupture scenarios generated for this study produce relatively lower ground motion at short

distances. The limited number of rupture scenarios considered in this study is not enough to support the investigation of the amplitude discrepancy observed here. The investigation of ground motion differences between the simulations and empirical models requires additional simulations using several realisations of the 1D crustal model and an extended suite of rupture scenarios covering a larger model parameter space, including the rupture area, and rise time, which could play a significant role in the ground motion amplification pattern on a broad frequency range. For example, simulations with a smaller rupture area, relative to the average rupture area adopted in this study, are expected to produce larger ground motion.

In addition to the direct comparisons with the GMMs we investigated the deviation of our simulated data from the GMMs by computing ϵ; a normalized measure of simulated ground motion intensity deviation from the median value predicted by the GMMs. ϵ is the natural log ratio of ground motion intensities (GMI's) normalized by standard deviation:

$$\epsilon = \frac{ln(z) - ln(\hat{z})}{\sigma}$$

z = simulated GMI

$\hat{z}$ = median GMI from the GMM for this event, path, site, etc…

σ = ln standard deviation of $\hat{z}$ (already in ln units)

ϵ of +/-1 means GMI is σ above/below median GMI estimated from the GMM

Small ϵ means the simulated GMI is very similar to the GMI predicted by the GMM. Figure 7 illustrate the variation of ϵ with the response period obtained for simulations with the two selected rupture models with different slip distributions. The very low epsilon values is another demonstration of the very good performance of our simulations. The synthetic ground motion has very similar characteristics with the GMMs at all considered periods and distances.

At the response period of 0.3s the standard deviation of GMI's from these selected ruptures with different slip distributions can be as high as 0.6 natural logarithm units (nearly a factor of two) for sites with a fault distance of 2km, but are much lower, closer to 0.2, for longer periods and at longer distances. This analysis demonstrates a breakdown of the ergodic assumption commonly used in GMM's and suggests that a distant and period-dependent sigma may better represent expected GMI's for seismic hazard calculations.

SA (0.5s)

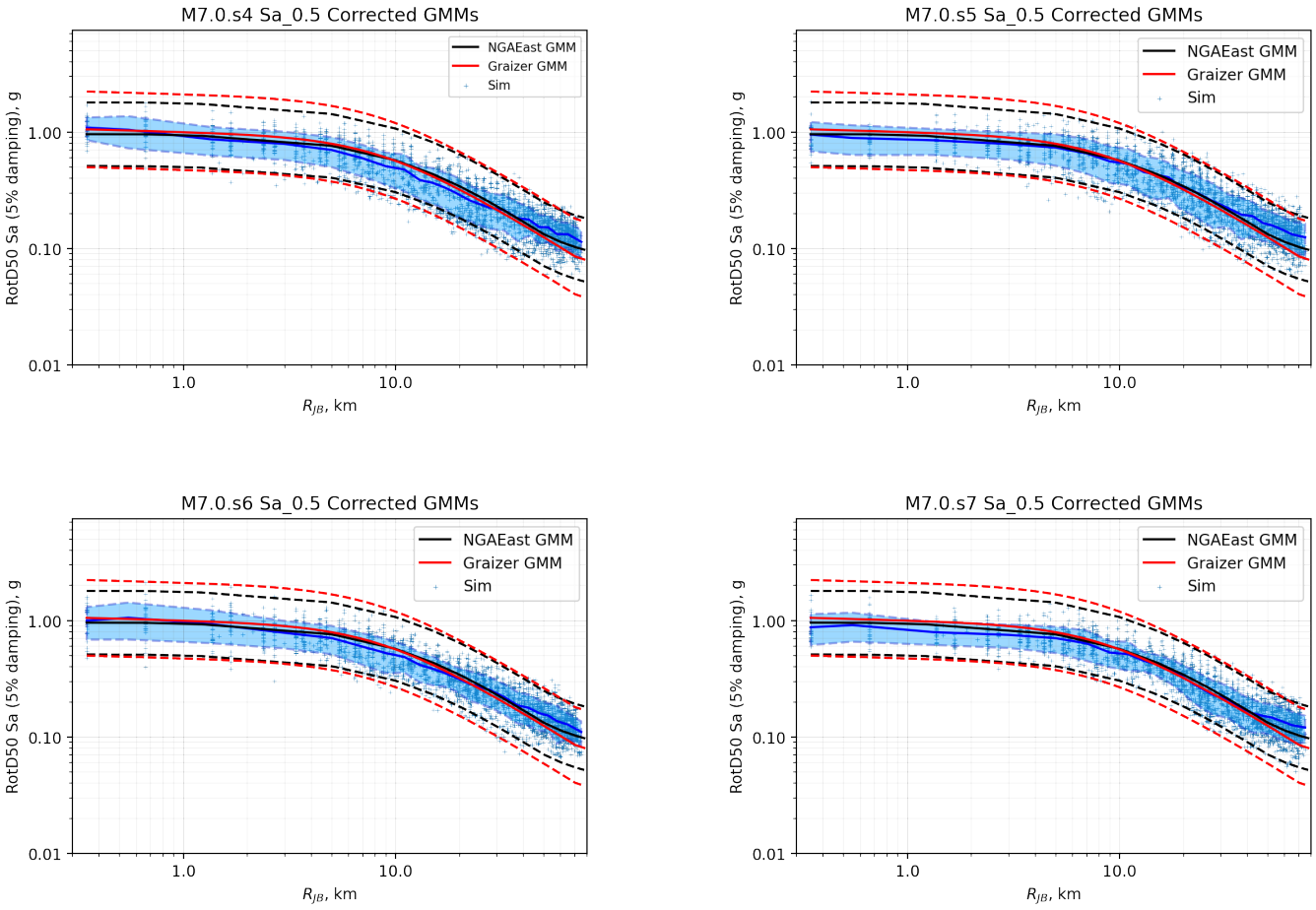

Figure 5a. Effects of slip distribution. Comparison of the RotD50 SA GMMs for the NGA-East model (black trace) and G-16v2 (Graizer, 2017) (red trace) with the computed RotD50 SA (blue trace) obtained for four different rupture models for which only the slip distribution was varied (blue crosses) and the other rupture parameters were kept the same. Each panel shows the comparison for each rupture model. The Rotd50 SA is computed for the spectral period of 0.5s.

SA (1.0s)

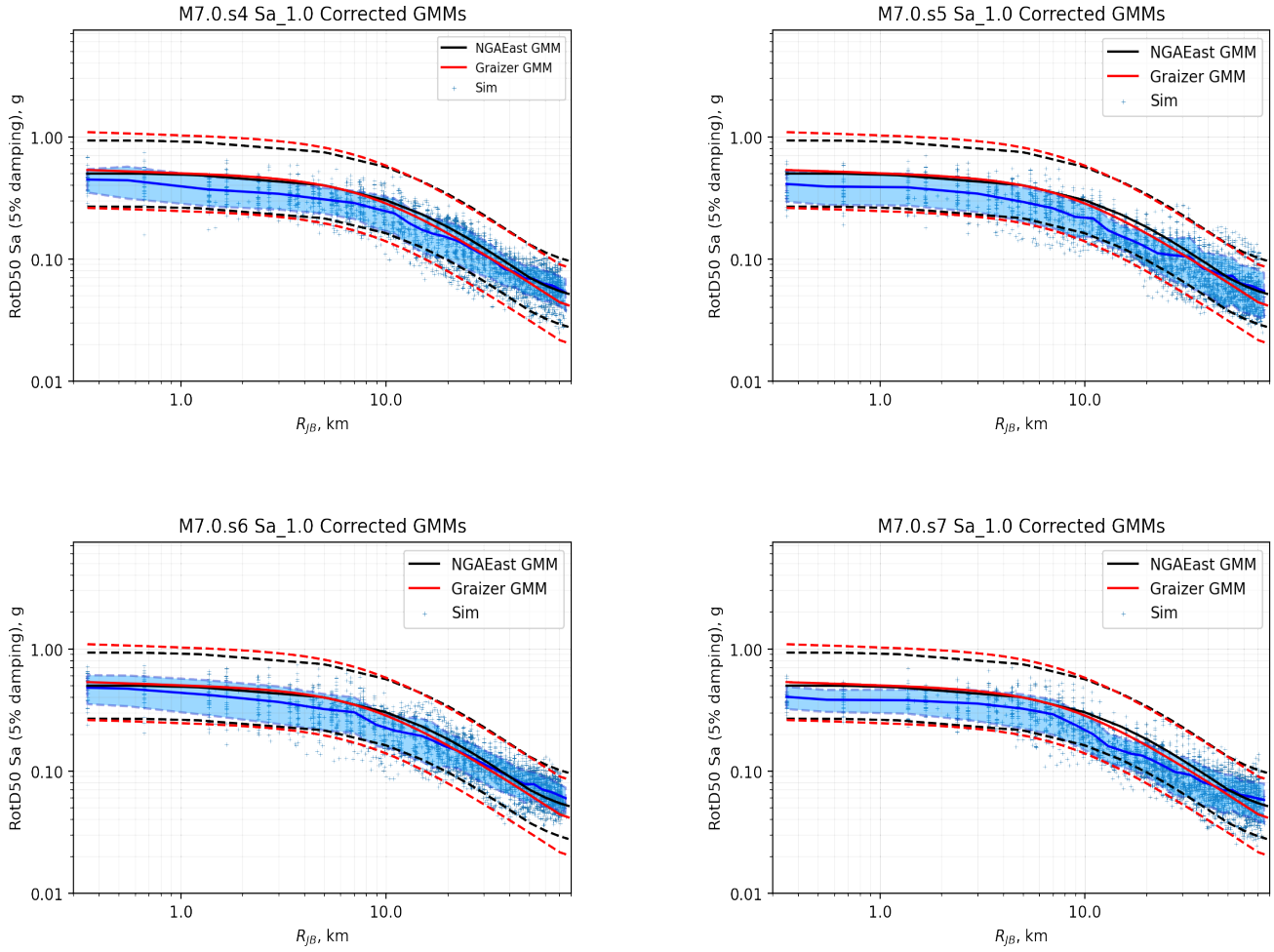

Figure 5b. Same as Figure 5a but for Rotd50 SA computed at 1.0s

SA (2.0s)

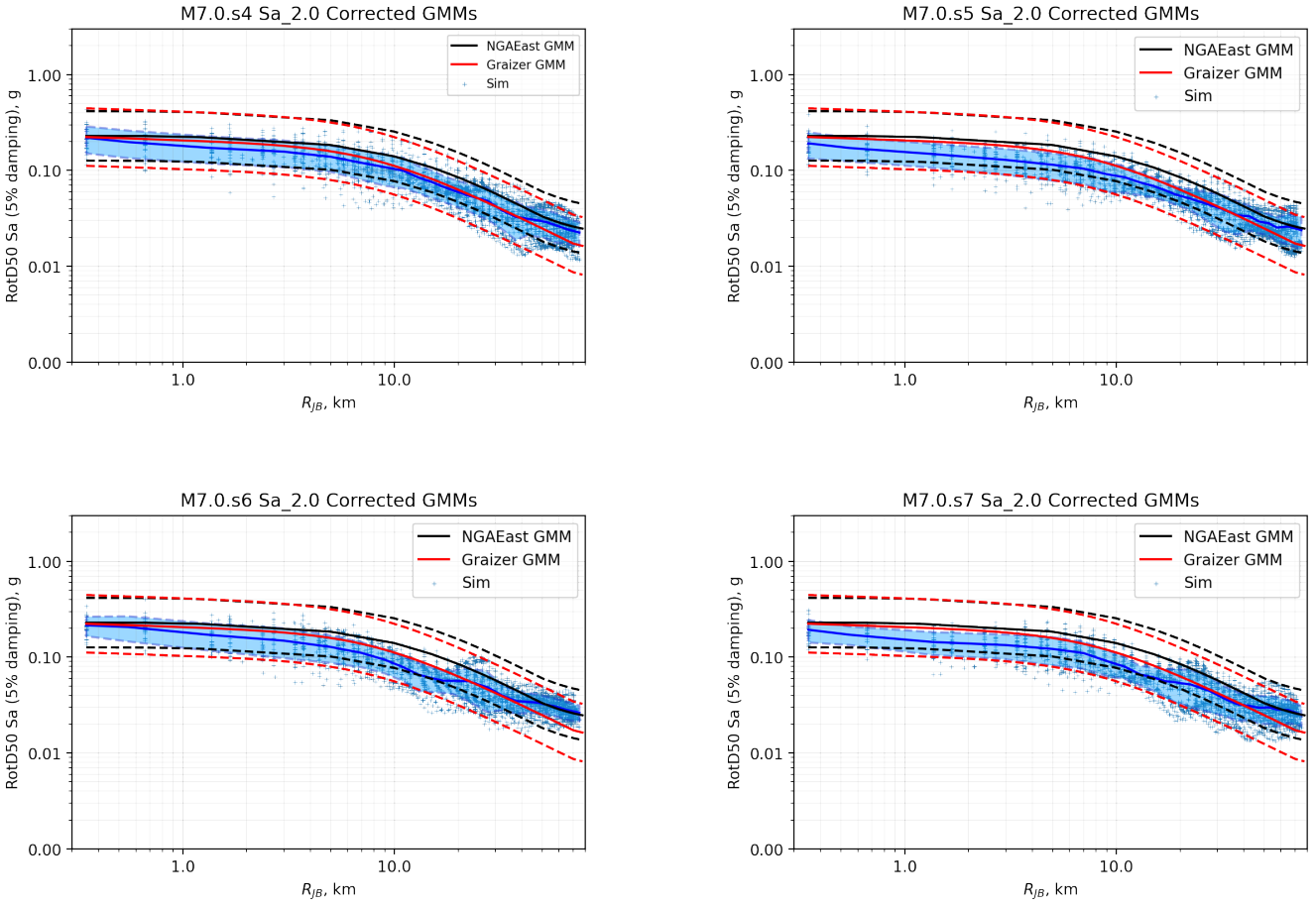

Figure 5c. Same as Figure 5a but for Rotd50 SA computed at 2.0s

SA (5.0s)

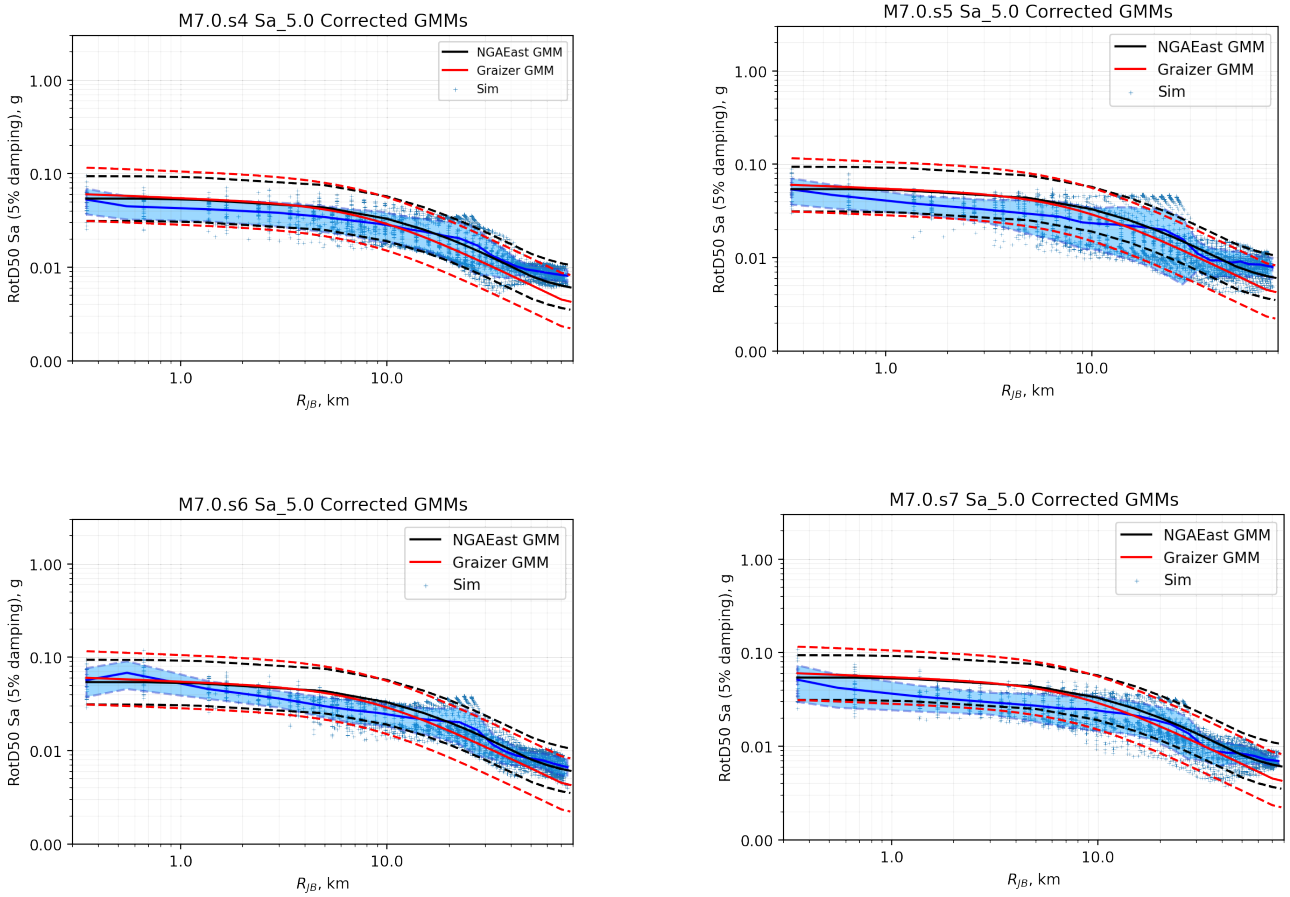

Figure 5d. Same as Figure 5a but for Rotd50 SA computed at 5.0s

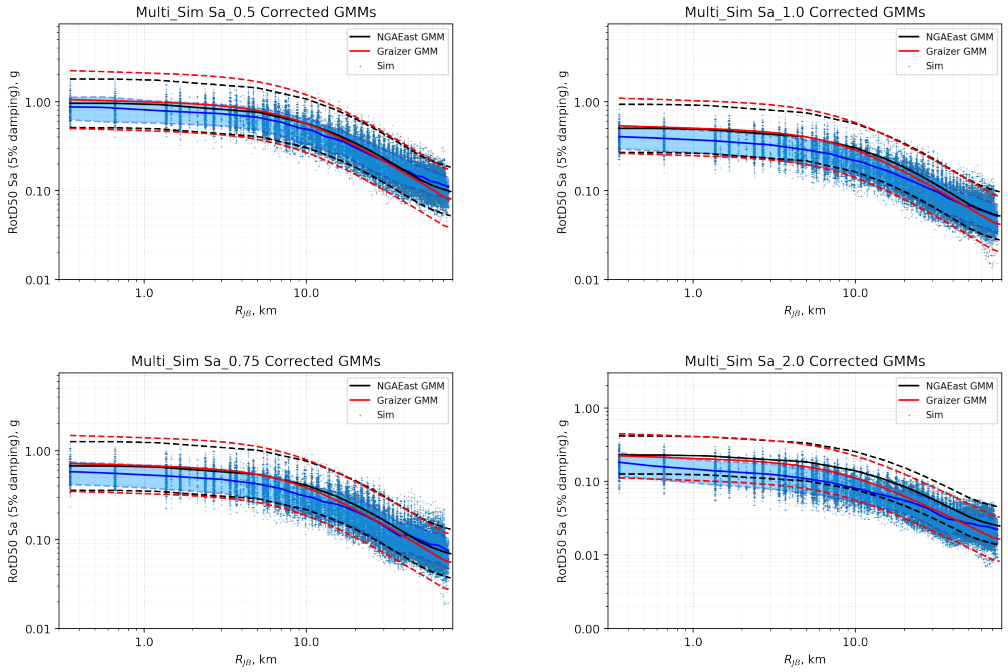

Figure 6a. Comparison of the RotD50 SA GMMs for the NGA-East model (black trace) and G-16v2 (Graizer, 2017) (red trace) with computed RotD50 SA (blue trace) obtained for all rupture models, excluding thrust rupture models. Each panel shows the comparison for the spectral periods 0.5s, 0.75s 1.0s, and 2.0s.

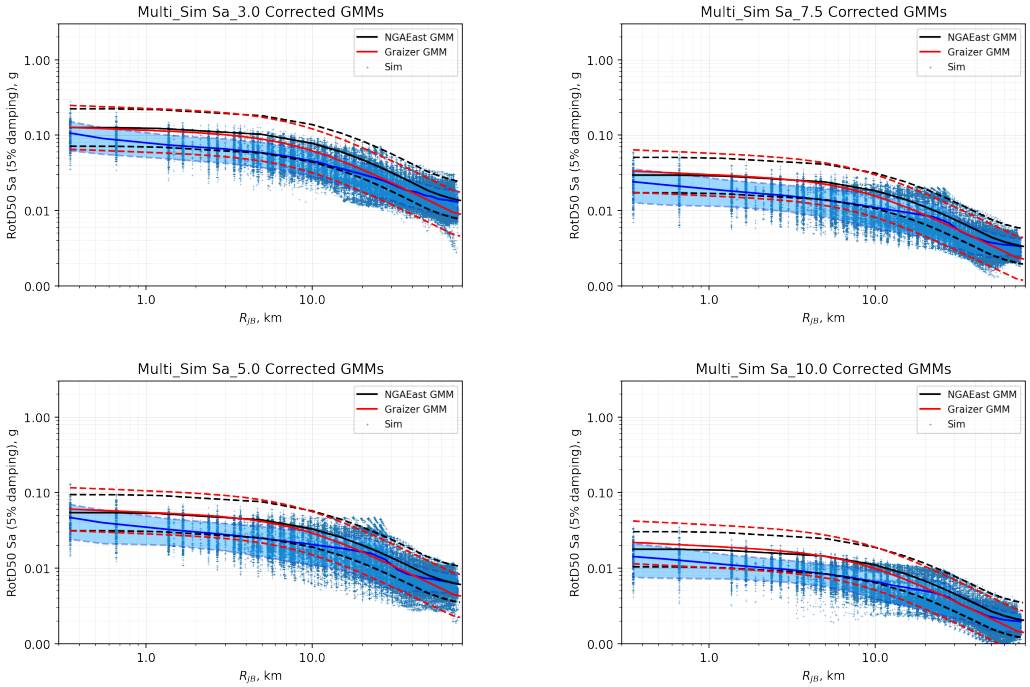

Figure 6b. Same as Figure5b, but for spectral periods of 3.0s, 5.0s, 7.5s, and 10s.

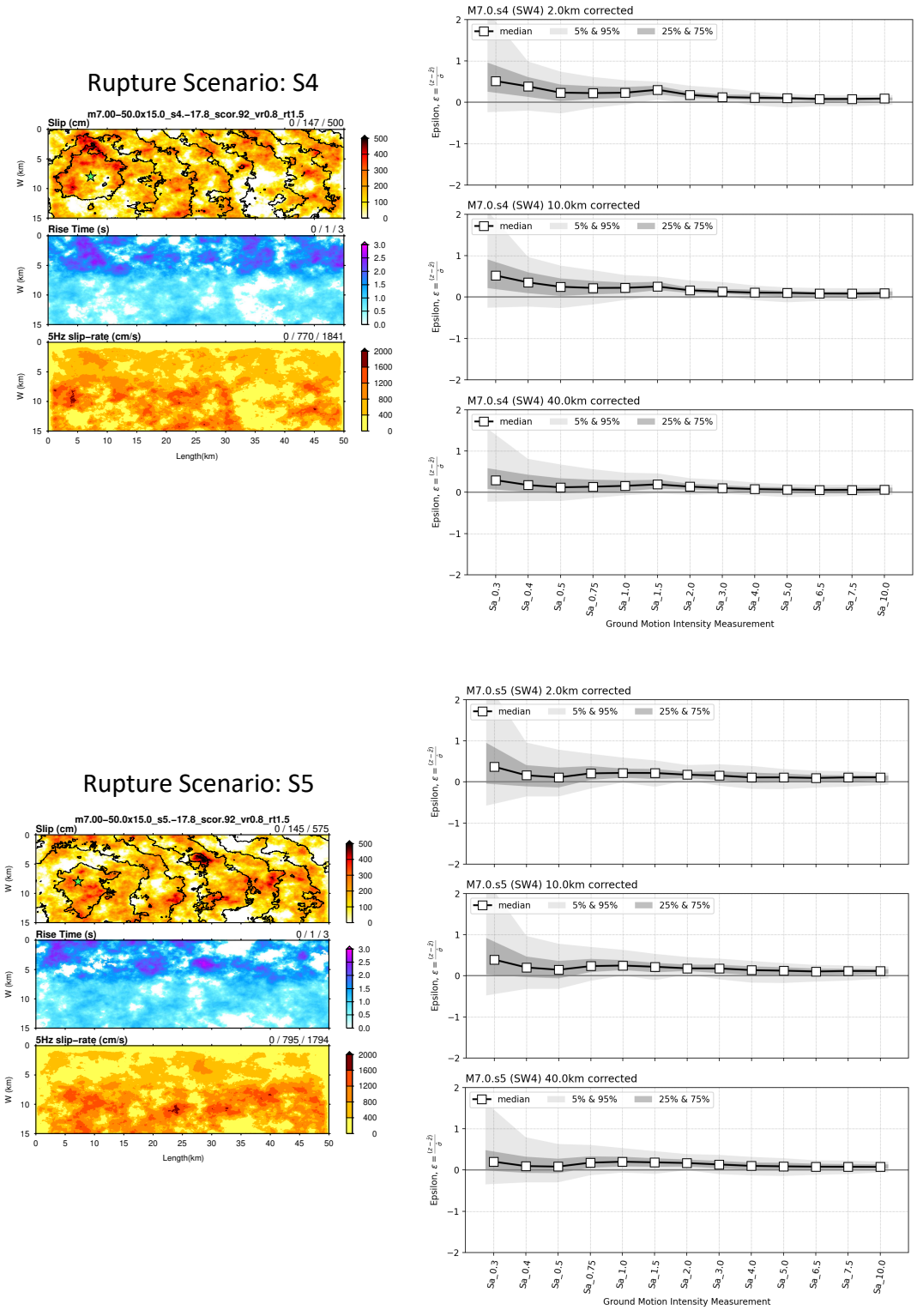

Figure 6. Illustrations of difference between the simulated and empirical SA using GMM G-16v2 (Graizer, 2017), expressed by ϵ; the natural log of difference between synthetic and empirical SA normalized the GMM standard deviation computed for model S4 (top panels) and model S5 (bottom panels). Left panels show the rupture model used in the simulations and the right panels show ϵ as a function of period for the R_{jb} distance of 2km (top ϵ panel), 10 km (middle ϵ panel), and 40 km (bottom ϵ panel).

We continued performance analysis of our simulations by focusing on the sensitivity of the simulated ground motion to rupture model parameters, mainly using comparisons with the Graizer's GMM, version G-16v2 (2017), considered as a reference model. We started investigating the rupture velocity effects. Figure 7 shows maps of simulated peak ground motion velocity (PGV), and peak ground motion acceleration (PGA) obtained for rupture velocities Vr=0.60Vs, 0.65Vs, 0.70Vs, and 0.75Vs. The PGV maps indicate that increasing the rupture velocity increases the PGV in the direction of the rupture propagation. This is a clear demonstration of increased rupture directivity effects expressed by a steady increase of the ground motion amplitude when the rupture velocity get closer the local shear wave velocity Vs. The rupture directivity effects have been observed during several California earthquakes such as the Mw 6.6 1971 San Fernando (McGuire and Hanks, 1980), Mw 5.7 1979 Coyote Lake (Archuleta, 1979) and Mw 6.5 1979 Imperial Valley (Swanger et al., 1981). The ground motion amplification due to the rupture directivity effects is larger on the fault normal component, especially at long and intermediate periods (> 1s) and for large rupture velocities, close the shear wave speed. Figure 8 compares Graizer's GMM, for the Rotd50 SA at periods 0.5s and 1s, with ground motion computed for four rupture models with different average rupture velocities, including Vr=0.60Vs, Vr=0.65Vs, Vr=0.70Vs, and Vr=0.75Vs. It is clear from these comparisons that simulations with a low rupture velocity (smaller than Vr=0.75Vs) consistently generate lower high frequency ground motion than the GMM. This result suggests that the proposed CEUS GMMs can be matched by simulations using a rupture velocity that is at or above Vr=0.75Vs. This is consistent with the conclusion of a recent study of recorded earthquakes that often large crustal earthquakes rupture with a super shear rupture velocity. On the other hand, the ϵ obtained for these four simulations, shown in Figure 9, remain relatively low at periods above 1s, which indicates that at long periods the difference between the simulations and the GMM is not very sensitive to rupture velocity.

In addition to simulations of strike-slip earthquakes we performed simulations of Mw7.0 thrust earthquakes for 4 rupture scenarios with dip angles of 80^o and 70^o and a rake angle of 90^o (pure thrust mechanism) and 70^o (thrust mechanism with a small strike slip component). The average rupture velocity was kept at 0.80Vs. The comparison of the RodD50 SA computed for all 4 rupture scenarios with the G-16v2 GMM (Graizer, 2017) is shown in Figure 10. The use of different thrust mechanisms leads to a considerable difference in ground motion amplitude at all periods. This is clearly seen in Figure 10, which also indicates that our rupture scenarios produce ground motion with slightly lower amplitudes than the G-16v2 GMM. The PGV and PGA maps shown in Figure 1, obtained for dip angles of 80^o and 70^o demonstrate the expected thrusting mechanism effects manifested as increased ground motion in the hanging wall side of the fault, compared to that on the footwall side. The effect is visible along the entire length of the fault in a narrow

region and increases for the shallower dip angle of 70°. This near-fault amplification can be explained by potential wave interactions with the free surface and upward rupture directivity effects, as well. It is interesting to note that similarly to the strike slip faulting our simulations of the thrust-faulting effects suggest that the ground motion amplitude from an Mw 7.0 crustal earthquake saturates at short distances and at all periods. As it is demonstrated in Figure 13, which compares RotD50 SA averaged over 10 rupture scenarios computed for strike-slip faulting and thrust faulting, this trend is different for Mw 6.5 thrust earthquakes for which the simulations produce a significant under saturation at short distances.

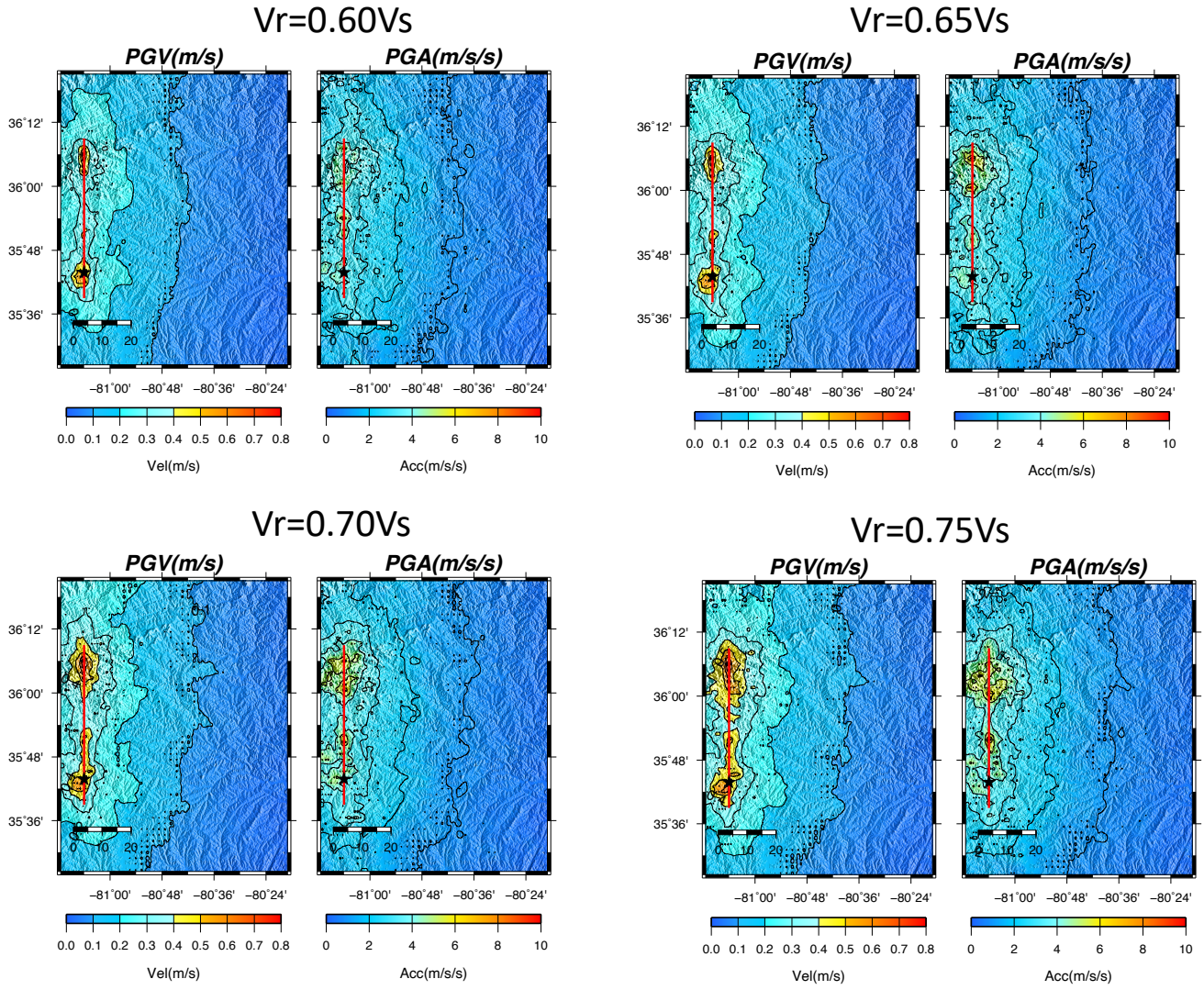

Figure 7. Effects of rupture velocity Vr on simulated ground motion (0-10Hz) for a M_w 7 strike slip earthquake. Maps of simulated PGV and PGA for Vr=0.60Vs, 0.65Vs, 0.70Vs, and 0.75Vs. The fault trace is indicated by the red line and the epicenter is indicated by the black star. PGV shows elevated values in the forward rupture directivity direction.

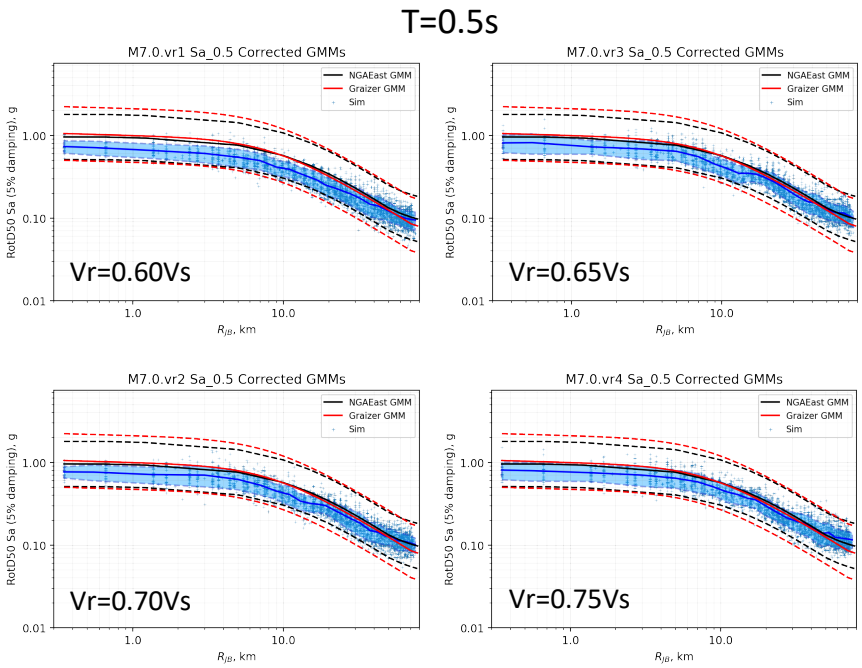

Figure 8a. Effects of rupture velocity Vr. Comparison of RotD50 SA GMMs for the NGA-East model (black trace) and G-16v2 (Graizer, 2017) (red trace) with the computed RotD50 SA (blue trace) obtained for four different rupture models for which only Vr was varied (blue crosses) and the other rupture parameters were kept the same. Each panel shows the comparison of Rotd50 SA for Vr=0.60Vs, 0.65Vs, 0.70Vs, and 0.75Vs, at 0.5s.

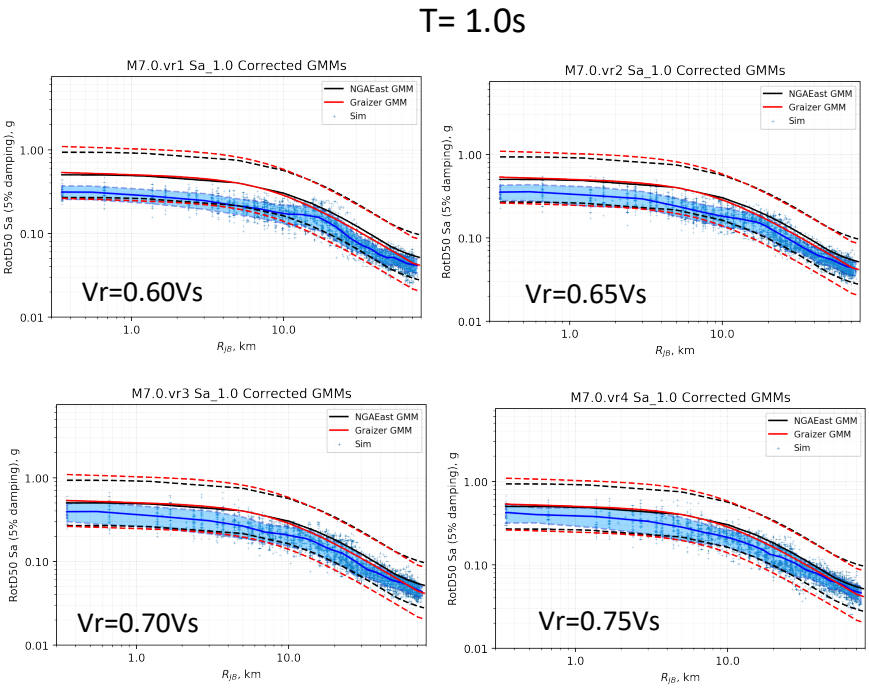

Figure 8b. Same as Figure 8a, but at T=1.0s

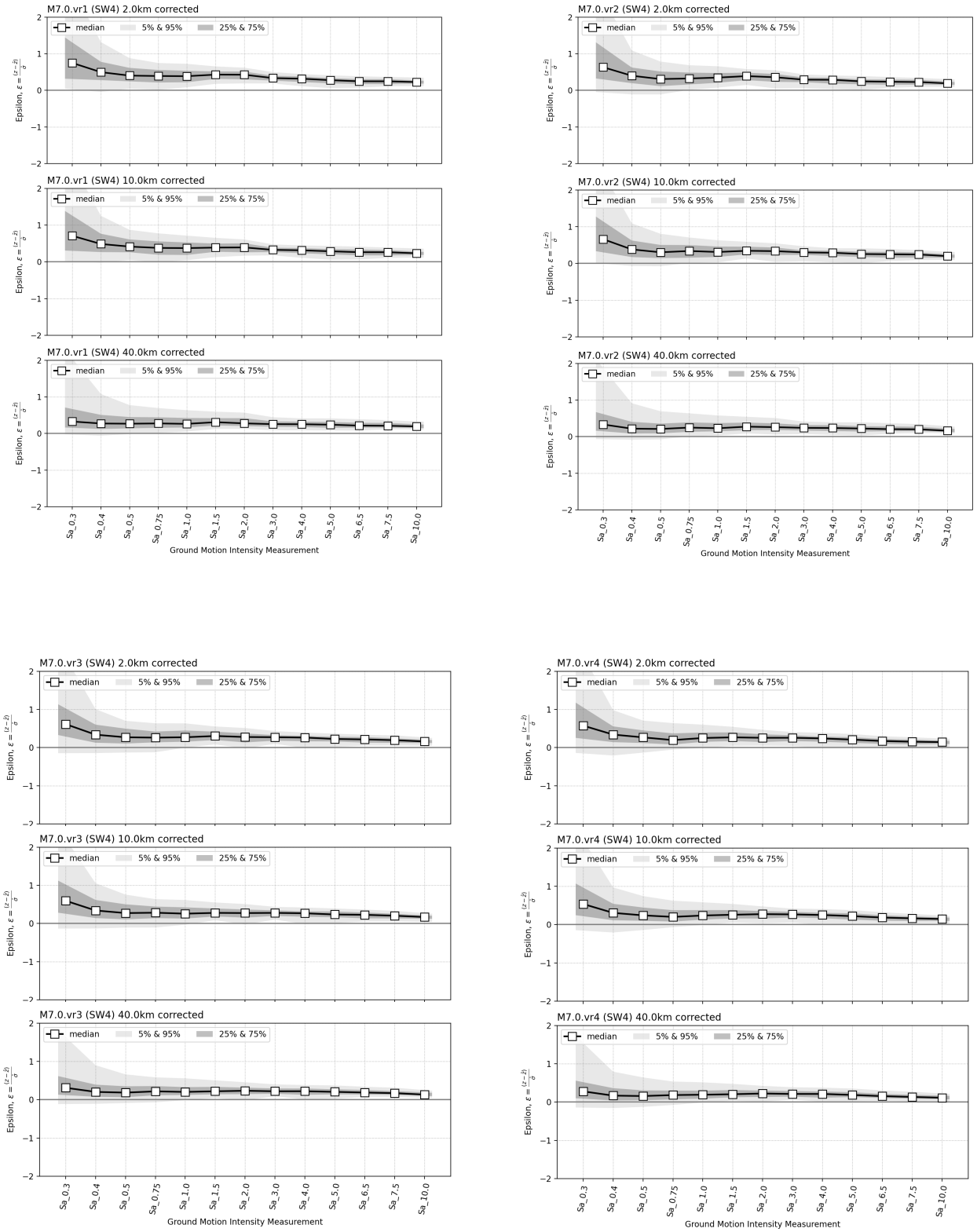

Figure 9. Difference between the simulated and empirical SA using GMM G-16v2 (Graizer, 2017), expressed by ϵ as a function of period for the R_{jb} distance of 2km, 10 km, and 40 km, computed for simulations obtained with Vr=0.60Vr (top left panel), Vr=0.65Vr (top right panel), Vr=0.70Vr (bottom left panel), Vr=0.65Vr (bottom right panel).

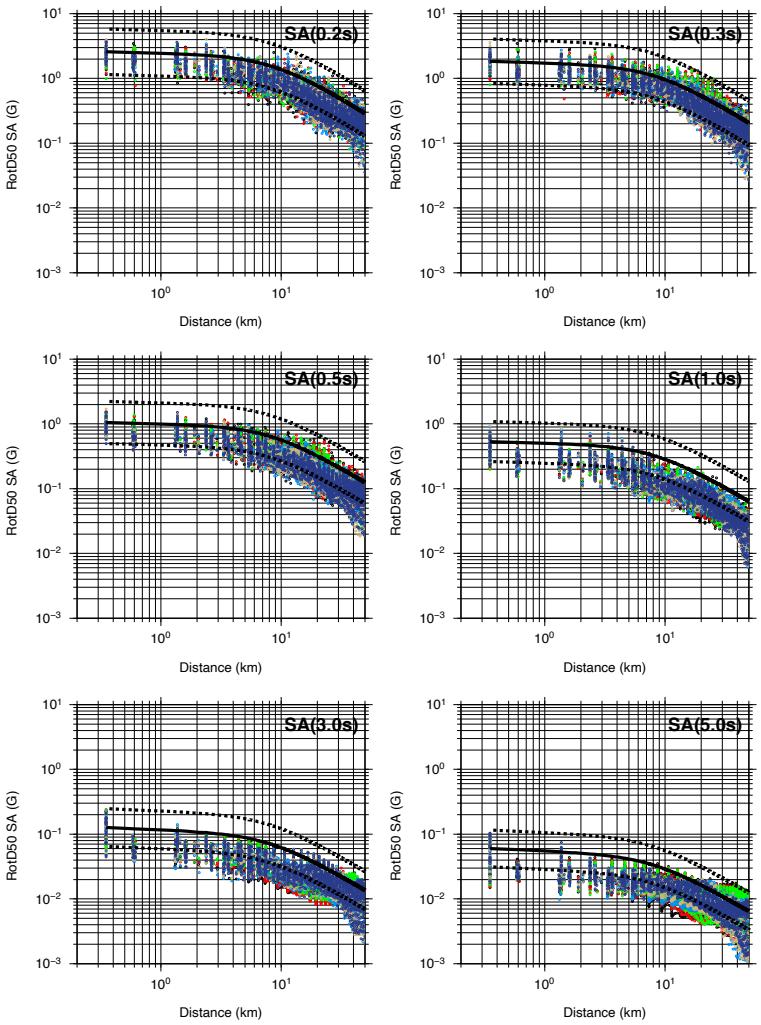

Figure 10. Comparison of RotD50 SA GMMs for the G-16v2 (Graizer, 2017) (red trace) with the computed RotD50 SA (coloured dots) obtained for four different rupture models for which only the faulting mechanism was varied, and the other rupture parameters were kept the same. Each panel shows the comparison for different spectral periods indicated on top of each panel.

4.0 NEAR-FAULT GROUND MOTION SATURATION AND ITS SENSITIVITY TO RUPTURE KINEMATICS

So far, we have demonstrated that the simulated ground motion and the adopted regional 3D velocity model produce ground motion characteristics that are in line with ground

motion predicted by empirical models for Mw6.5 and Mw7.0 crustal earthquakes. After gaining confidence in the ability of the simulation technique to produce reliable results we used simulations to investigate ground motion characteristics at near-fault distances where the GMMs are poorly constrained. In our investigation we used a series of simulated ground motion produced with a suite of rupture realizations obtained by varying several rupture parameters within plausible ranges that are known to affect the ground motion.

4.1 Near-Fault Saturation

The near-fault ground motion saturation (0 to 5 km from fault rupture) for moderate and large earthquakes is a subject of current research. Its investigation is hindered by the sparsity of strong motion recordings, especially for large earthquakes with normal and thrust faulting. Despite new strong-motion data recorded from recent earthquakes, there is still not sufficient data that can uniquely prove hypotheses about the behavior of strong-motion attenuation function in the near field used in proposed GMMs (, 2018). Differences in constraints applied to the near-fault saturation models result in significant differences between empirical near-fault ground motion prediction

This is demonstrated in Figure 13 which compares different GMMs for the SA at 1s for the 5.25<Mw<5.75 range. The comparison highlights the relative difference between the predicted SA which could be as high as a factor of 2. On the other hand, abundant data for smaller magnitude events clearly show that near-fault ground motion for small magnitude earthquakes does not saturate at short distances (Atkinson and Viegas, 2023). A typical example of an Mw2.8 earthquake is shown in Figure 13. The recorded data for this earthquake suggest that the ground motion decay with distance is log-scale linear. The controversial hypothesis that a similar pattern may be observed for all magnitude has not found support among many GMMs modeler. Moreover, although very sparse, an increasing number of ground motion records of large earthquakes confirm the saturation hypothesis. Physics-based ground motion simulations using a deterministic approach, as the one performed in this study, can be used to guide the extrapolation of observed near-faut ground motion attenuation for small earthquakes to that for intermediate and large earthquakes using simulations. Numerical modeling can also be used to separate the rupture and wave propagation effects that are significant contributors to the near-fault attenuation for extended sources.

We used synthetic ground motions computed for over 60 rupture scenarios to investigate the ground motion amplitude saturation at short distances from the fault.

Figure14 illustrates the simulated ground motion amplitude saturation. In this figure we compare the simulated and predicted RotD50 SA by Graizer's G-16v2 GMM for Mw6.0, Mw6.5, and Mw7.0 strike slip earthquakes for CEUS. As indicated by red arrows the slope of the near-fault saturation of the spectral response at short distances for strike-slip earthquakes is magnitude dependent. We note that the predicted near fault saturation by

Graizer's G-16v2 GMM is very similar to the one produced by our simulations for Mw7.0 earthquakes.

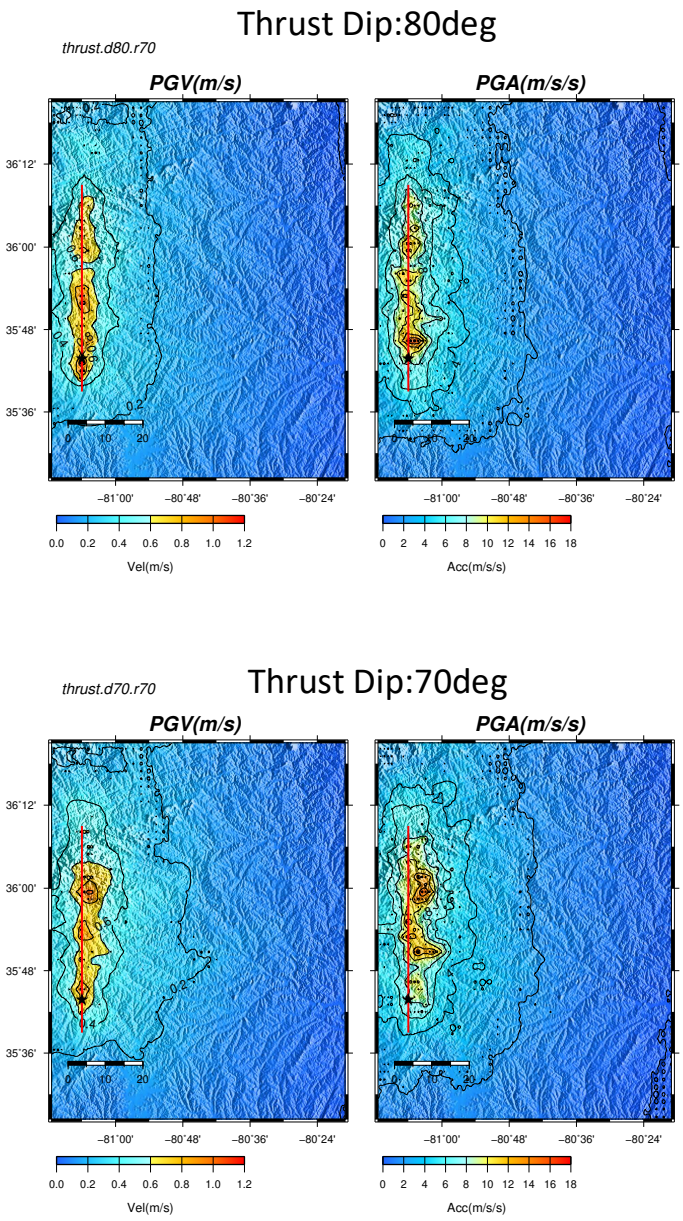

Figure 11. Effects of dip angle on simulated ground motion (0-10Hz) for a *Mw*7 thrust earthquake. Maps of simulated PGV and PGA for fault dip angles of 80 degrees (top panels) and 70 degrees (bottom panel). The fault trace is indicated by the red line and the epicenter is indicated by the black star. PGV and PGA on the hanging wall side of the fault are higher for the shallower dip angle of 70 degrees.

For the Mw6 and Mw6.5 earthquakes the simulations produce a slight undersaturation that is not predicted by the G-16v2 GMM. A similar difference in near-fault amplitude saturation is seen in comparison with the CEUS GMM. Our simulation results suggest

that the near-fault undersaturation becomes more pronounced at magnitudes smaller than Mw6.5.

The near-fault saturation is a robust feature of ground motion that does not depend on specific kinematic rupture characteristics. The simulated near-fault ground motion saturation supports findings in several studies that attribute the saturation to the radiation pattern effects combined with wave propagation effects (e.g. Chapman and Godbee, 2012; Baumann and Dalguer, 2014). It has been argued that for large earthquakes saturation can be a result of several factors, including the local source radiation pattern, rupture directivity, low-velocity fault zone scattering (e.g., Li and Vidale, 1996), and nonlinear soil response. For long faults the oversaturation is a direct consequence of the definition of the source distance as closest distance from the fault plane. The closest distance to the fault does not necessarily represent the distance from the most energetic part of the fault rupture. The so-called strong motion generation areas are often relatively deep, and in the case of large earthquakes they are concentrated in distributed small areas with high stress drop. Consequently, as shown by our simulations, their cumulative effect on ground motion time history is stronger at stations away from the fault where the wave generated from these energetic parts of the fault are more coherent, as opposed to short fault-distance locations along the fault trace.

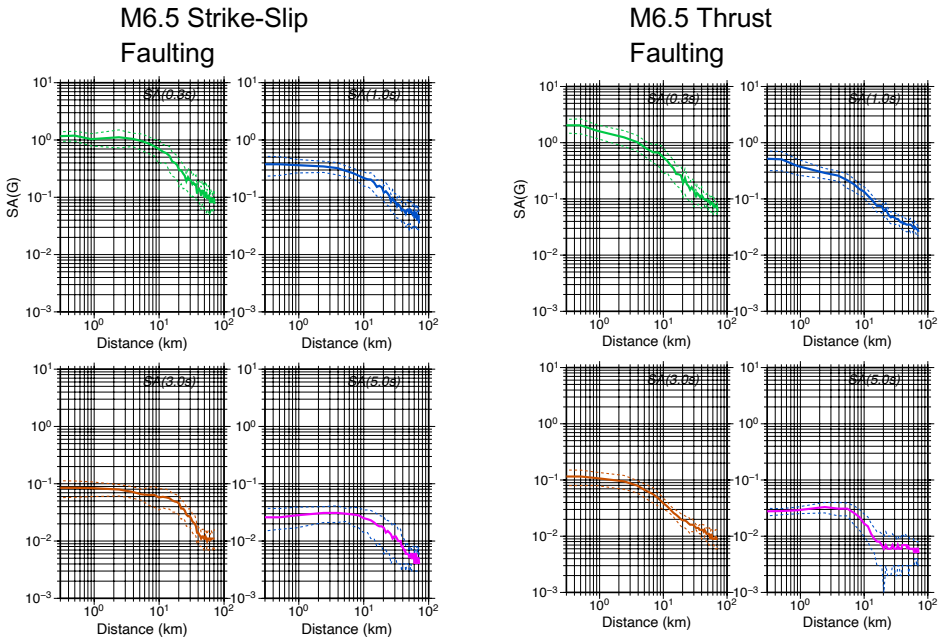

Figure 12. Ground motion amplitude saturation for strike slip-faulting (left panels) and undersaturation for thrust-faulting (right panels) for M6.5 scenario earthquakes. Computed RotD50 SA averaged over 10 rupture models for which only the slip distribution was varied, and the other rupture parameters were kept the same. Each panel shows the average and +/- 1 standard deviation of the RotD50 SA at different spectral periods, indicated on top of each panel

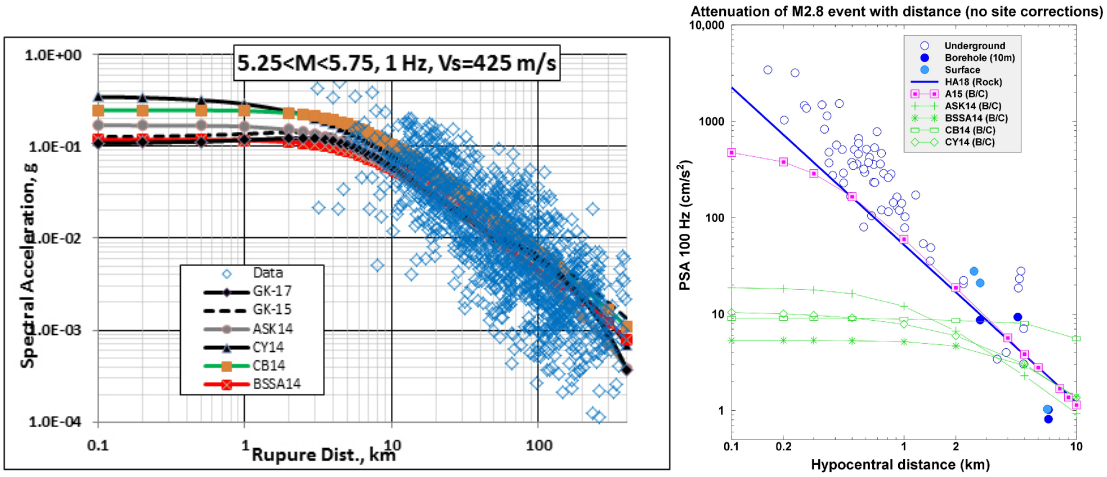

Figure 13. Near-fault ground motion saturation. Left Panel: GMMs for the SA at 1s for 5.25<M<5.75. Rhombs are observed ground motion spectral accelerations. Right Panel: GMMs and recorded PSA for a M2.8 earthquake (Atkinson, Viegas, 2023)

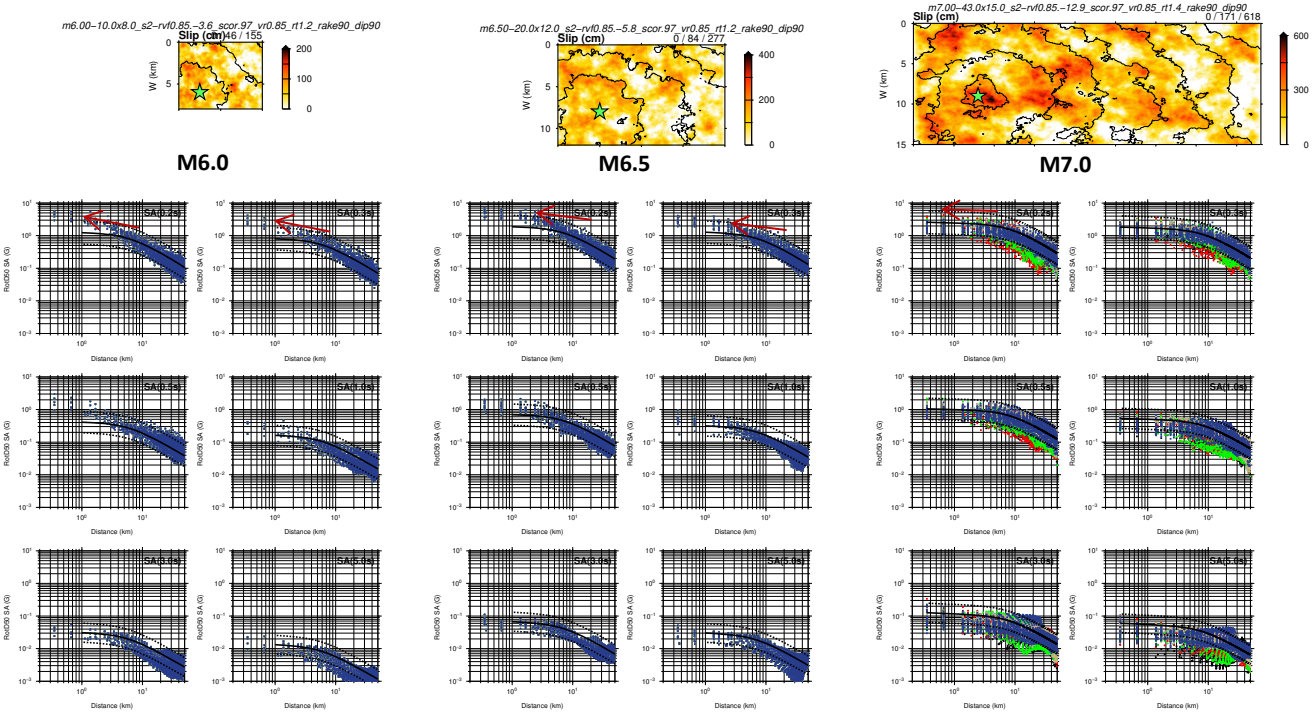

Figure 14. Simulated near-fault ground motion saturation. Comparison of simulated (coloured dots) and predicted RotD50 SA by Graizer's G-16v2 GMM **(**black traces) for M6 (left panels), M6.5 (centre panels), and M7.0 (right panels) strike slip earthquakes for CEUS. Examples of slip models generated with the GP method (Graves and Pitarka, 2015) for M6, M6.5, and M7 earthquakes, are shown on top of each panel. The red arrows indicate the slope of the near-fault saturation of the spectral response.

5. 10HZ GROUND MOTION SIMULATION OF THE M7.0 1886 CHARLESTON, SOUTH CAROLINA EARTHQUAKE

The Mw7.0 1886 Charleston, South Carolina earthquake is the largest historic earthquake in the United States, east of the Appalachian Mountains. The investigation of the causative fault and ground motion estimates for the earthquake is very important for the seismic hazard assessment in the region. Identifying the fault that ruptured during the earthquake is a long-standing quest in the earthquake hazards community (e.g. Pratt et al.,2022; Bilhum and Hough, 2023; Pratt et al., 2023). Most of the fault models relied heavily on the post-earthquake report by Dutton (1889), who suggested two epicenters, one about 10 km southeast of Summerville and the other a few kilometres west of Rantowles. Thorough investigations, including reported buckled rails, buildings damage, extensive liquefaction features, and other surface soil damage distribution, south of Ashley reiver indicate for strong ground shaking 40km south from east of Summerville to southwest of Rantowles, potentially generated by a west dipping blind fault (Pratt et al., 2024). Based on analysis of the damage reports, the local seismicity recorded by a temporal local network, geological data on shallow subsurface structure, and seismic reflection profiles, Chapman et al (2016) and T. Pratt (personal communication) propose a rupture on a blind mid-crustal fault, striking south and dipping to the west that generated an earthquake with a Mw of about 7.0.

We used the Chapman et al. (2016) model of a south-striking fault extending from east of Summerville to west of Rantowles, as indicated in Figure 14, to simulate ground motion for the M7 Charleston earthquake and compare it with the observed damage zone. The rupture parameters used in the 10Hz simulations are shown in Table 2. As shown in Figure 15, the Chapman et al. (2016) model provides a reasonable working hypothesis for the 1886 fault rupture. Figure 15 shows the plots giving the static vertical displacements and Coulomb computed stress change. The area of the largest positive stress change coincides with most of the seismicity, which is consistent with the seismicity being primarily aftershocks from the 1886 earthquake.

Table 2: Parameters of the *preferred kinematic rupture model*

Magnitude: Mw=7.0
Fault length: 45 km
Fault width:12 km
Fault depth: 4.5 km
Strike angle: 186^{o}
Dip angle: 43^{o}
Rake angle: 124^{o}

We performed several 10Hz simulations using kinematic rupture models generated with the Graves and Pitarka rupture generator (GP) (Graves and Pitarka, 2016) and the fault location and geometry proposed by Chapman et al. (2016). The criteria for selecting a

preferred rupture model was the reproduction of the observed damage pattern shown in Figure 16, with the simulated ground motion amplification pattern. Figure 17 shows two preferred GP rupture models and maps of the corresponding simulated PGA and PGV, with ground motion amplification patterns closely matching the observed damage zone. These simulations demonstrate that, in order to obtain an area of large ground motion amplification located east of the fault trace, the fault needs to be dipping toward west with a relatively shallow dip angle. This is consistent with the Chapman et al. (2016) model. The shallow fault angle and the mixed strike and dip slip mechanism favour the upward rupture directivity effect that enhances the ground motion amplification toward the east. Also, compared to a bilateral rupture, a unilateral rupture with the rupture initiating at the southern end of the fault, produces a favourable ground motion amplification pattern that extends to the north, including the Summerville which was heavily damaged (see Figure 17).

A key feature of the proposed rupture model that controls the near-fault ground motion amplification pattern is the location of the large slip patch relative to the rupture initiation area. In general, the slip pattern of large crustal earthquakes is characterized by at least one shallow large slip area. As demonstrated by near fault ground motion recordings and dynamic rupture modelling the shallow slip ruptures mostly affect the low frequency of the generated seismic energy. Their spatial extent and their relative location to the hypocenter, play an important role in enhancing the forward rupture directivity effects which mainly amplify the ground motion along the fault and in the direction of rupture propagation. Our sensitivity analysis of the large slip patch effects on the simulated ground motion amplification pattern is shown in Figure 18. We concluded that a large slip patch and a hypocenter in the southern part of the fault are required to better match the simulated ground motion pattern with the observed damage pattern. A rupture model without large slip patches does not create enough focused energy to the east of the fault. Also, a slip patch located near the north end of the fault generates a very small zone of unrealistic extremely high PGV located outside the observed damage zone.

We concluded that a slip model with two large slip patches and a rupture initiation located near the southern end of the fault can generates ground motion that better matches the observed damage zone. In addition, as demonstrated by the velocity time history computed for Summerville, shown in Figure 19, a south hypocenter is needed to create a large velocity pulse known to create severe damage to low rise buildings. This is consistent with the large damage to buildings and the wide spread of the reported toppled chimneys in Summerville during the earthquake.

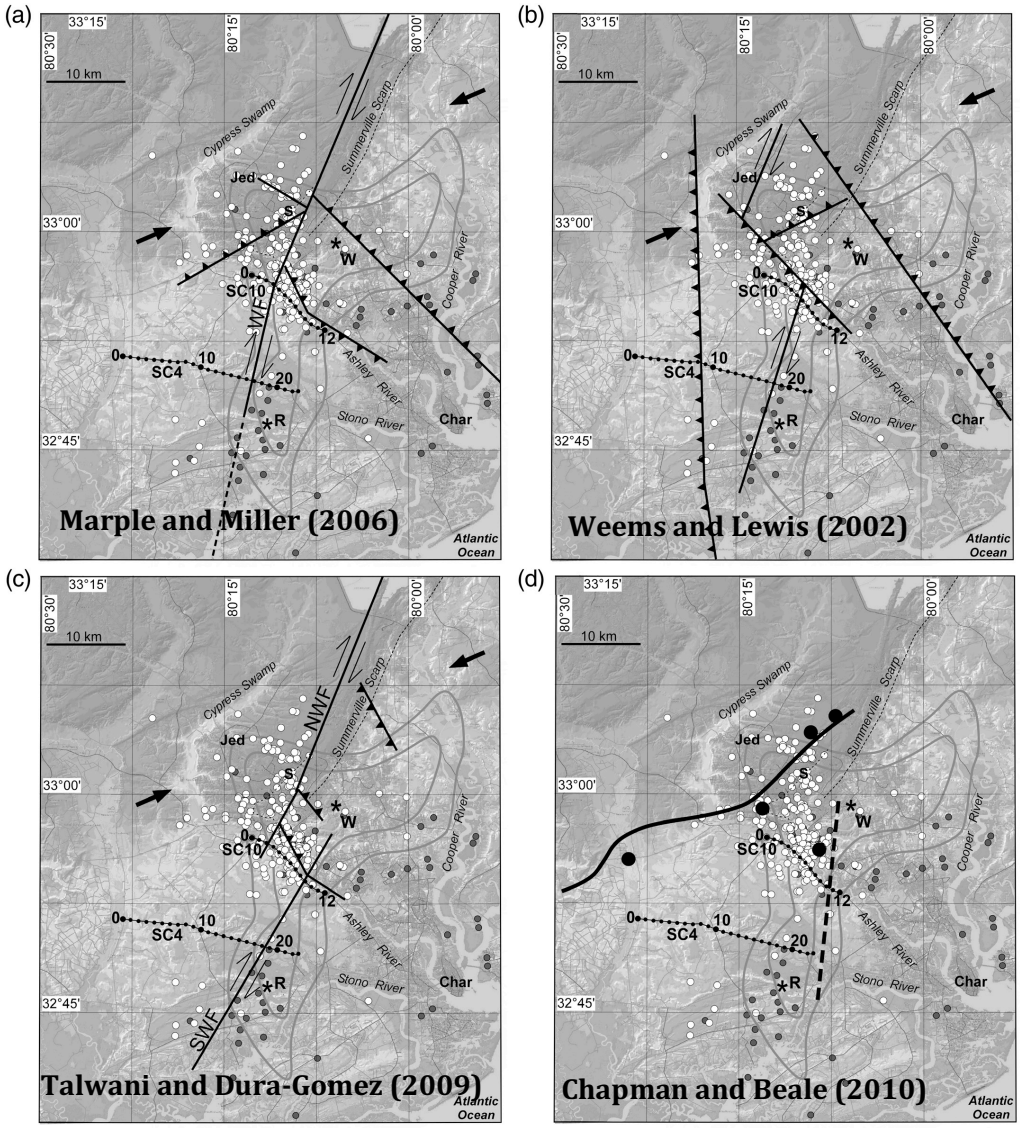

Figure 14. Local maps showing the proposed location of the causative fault segments (black solid lines) of the M7 1886 Charleston, South Carolina, Earthquake, and recent seismicity (white circles). In this study we adopted the fault location and geometry proposed by Chapman and Beale (2010).

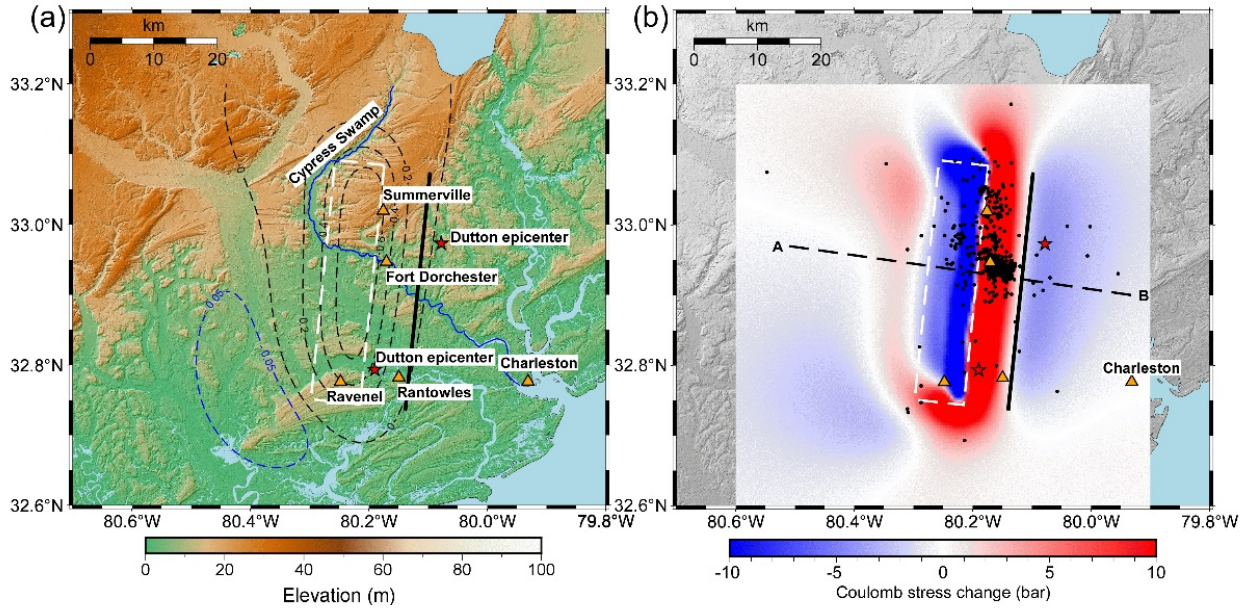

Figure 15. Left panel: Uplift pattern predicted by the Chapman et al. (2016) model for the 1886 Charleston earthquake, with dashed uplift contours in meters. The rupture is outlined by the white dashed rectangle and the heavy black line is the surface projection. Right panel: Coulomb stress change computed on planes coplanar with the rupture at a depth of 4.5 km. The area of largest positive stress change coincides with most of the seismicity (black dots), consistent with the seismicity being primarily aftershocks from the 1886 earthquake.

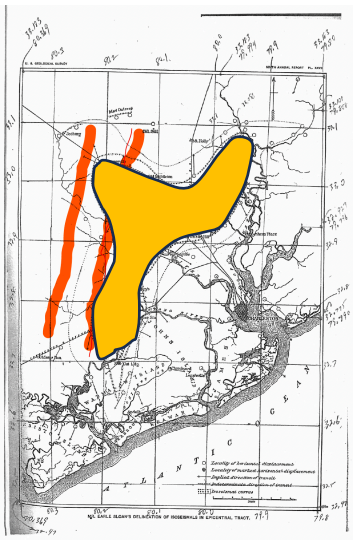

Figure 16. Local map of Soth Carolina showing the zone of observed strong shaking during the earthquake (yellow colour) and the surface projections of the top and bottom edges of the proposed fault (Chapman, personal communications).

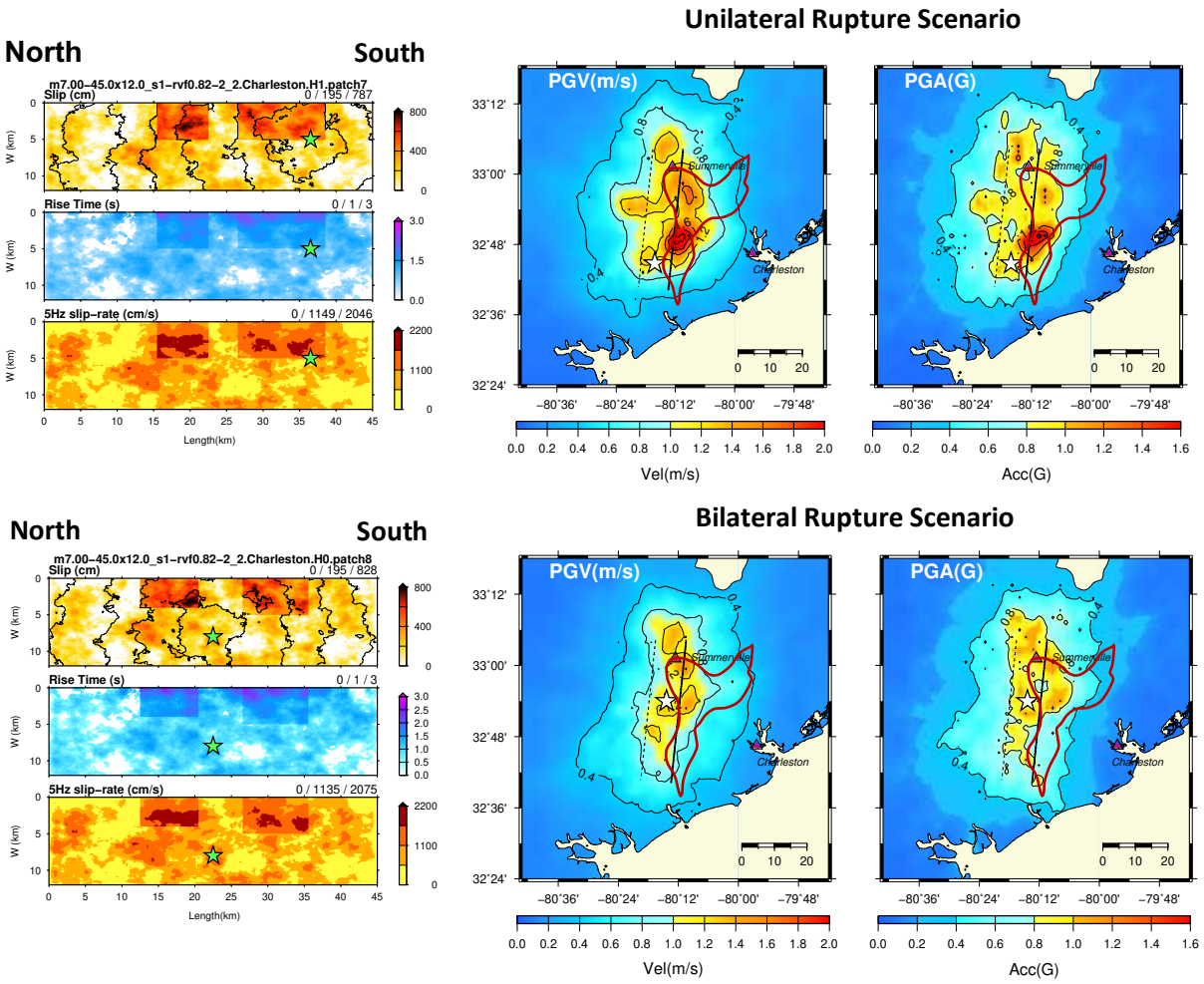

Figure 17. Preferred kinematic rupture models and 10 Hz simulated PGV and PGA maps of the M7 1988 Charleston earthquake. Left panels: Kinematic rupture modes generated with Graves & Pitarka rupture generator (Graves and Pitarka, 2015) for a unilateral rupture started near the south end of the fault (green star) (top panel) and a bilateral rupture model (bottom panel). Right panels: Simulated PGV and PGA maps for the unilateral rupture scenario (top panel) and bilateral rupture scenario bottom panel). Red line delineates the damage area observed during the earthquake.

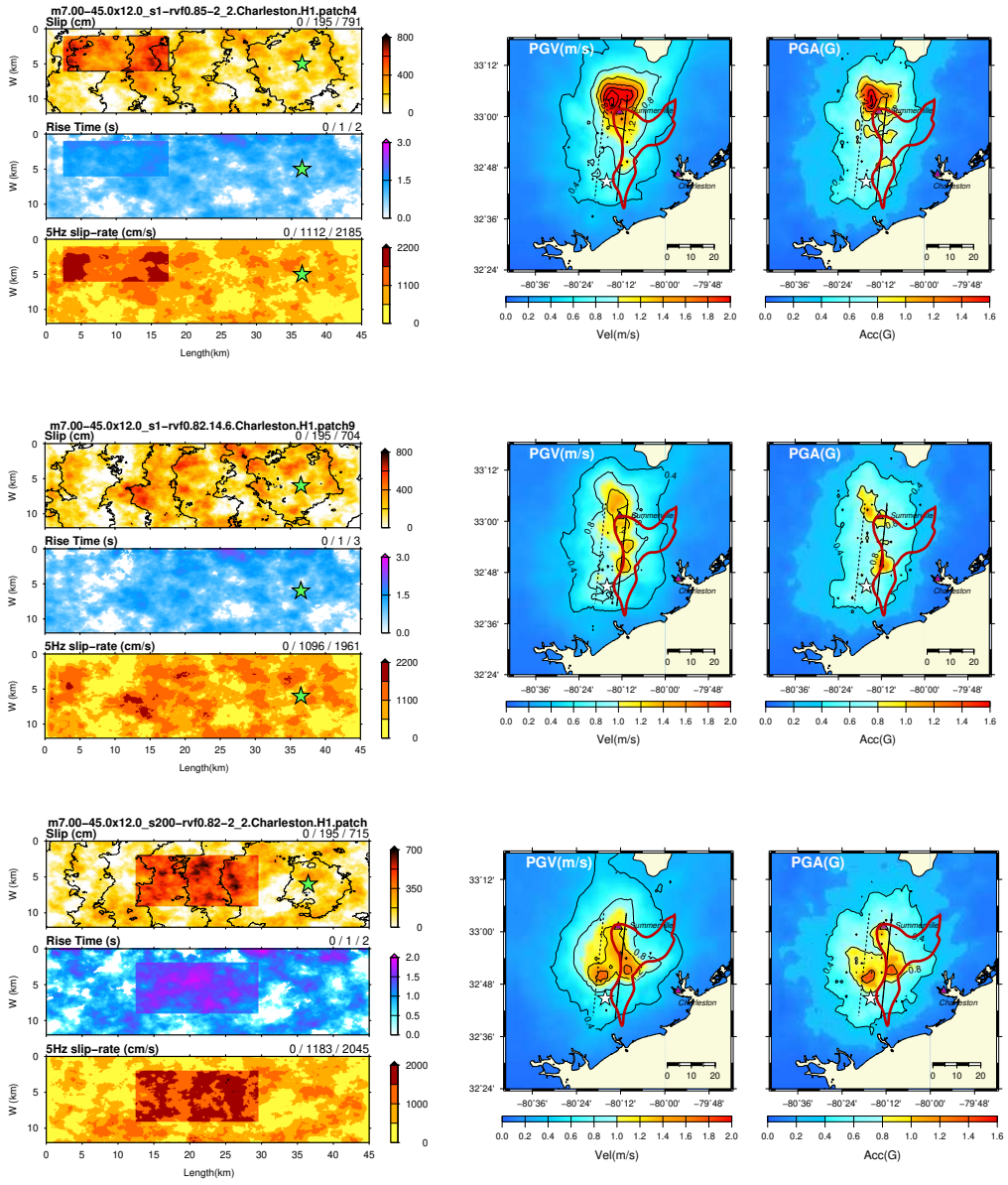

Figure 18. Simulated peak ground motion sensitivity to large slip patches in considered rupture models (left panels). PGV and PGA maps (right panels)

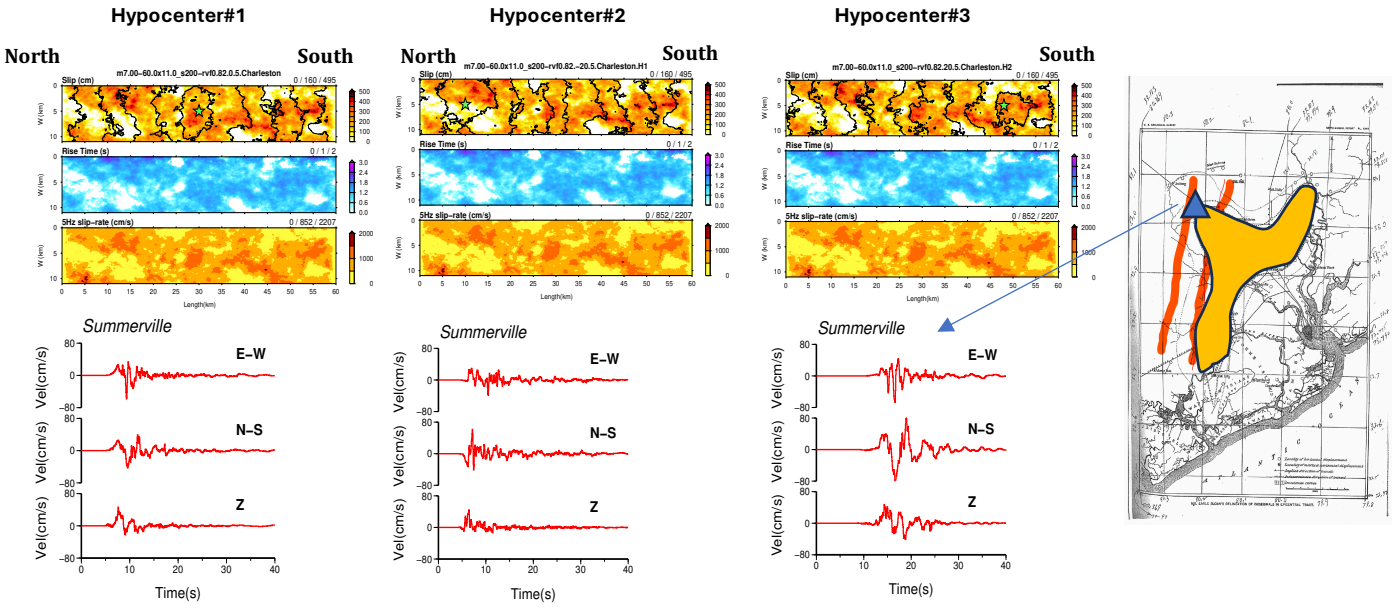

Figure 19. Simulated ground motion sensitivity to rupture initiations (green star). Top panels: Rupture scenarios. Bottom panels: Simulated three component ground motion velocity at Summerville. Sommerville's location is indicated by the blue triangle. Note the typical large pulse on the N-S component generated by the northward rupture directivity effect.

6.0 CONCLUSIONS

Physics-based earthquake simulations are rapidly finding applications in seismic hazard assessment and structural engineering, supplementing the available earthquake record databases, and creating unprecedented opportunities for GMM improvements, site-specific seismic analysis and design of NPP structures. Due to advances in understanding earthquake fault rupture processes and high-performance computing, the simulated earthquake ground motion incorporates significant realistic features on a broad frequency range (e.g., McCallen et al., 2022, Pitarka et al., 2020; Rodgers et al., 2019). The main objective of this project was to provide technical capabilities for producing physics-based ground motion that can be used to constrain the GMMs for Stable Continental Regions (SCR) at short distances and large magnitudes. Here we performed a feasibility study for the Mw7.0 strike slip scenario earthquakes simulated using the LLNL Broad-Band Simulation Platform customized for earthquakes in the US Stable Continental Region. Based on SW4, a highly efficient elastic wave propagation code, and the GP rupture generator, the LLNL physics-based simulation platform is well suited to high performance computing. LLNL's CPU and GPU based computing platform can be used to simulate ground motion for large crustal earthquakes and on a broad frequency range of engineering interest of up to 10Hz.

In an early stage of this study, we built a regional 3D velocity model for CEUS by combining the Saikia's 1D velocity model with correlated stochastic perturbations. The hybrid model enhanced the performance of the waveform modeling on a broad frequency range. The proposed model was validated using comparisons of simulated and recorded data from two local moderate earthquakes. The successful comparisons demonstrated the reliability of the 3D regional velocity model and the good performance of our deterministic simulation approach while emphasizing the importance of including small-scale variability in simulations of high-frequency wave scattering effects.

Additional validation analysis of the simulation platform, based on comparisons with different GMMs for a *Mw*7.0 earthquake in the CESUS region, resulted in a very good match between the simulated and empirical ground motion models. The successful validations against recorded earthquake and empirical ground motion models justifies the use of synthetic waveforms in analysis of ground motion characteristics, such as within and between event variability and near-fault amplitude saturation.

The initial investigation of within-event and between-event ground motion variabilities for the *Mw*7.0 scenario earthquakes on a strike-slip fault, suggests that they are strongly related to spatial slip and slip rate variations, average rupture velocity, rupture area and rupture initiation location.

Our simulation results suggest that the near-fault ground motion for an extended fault saturates at distances < 5km. Based on multiple realizations of the earthquake rupture, in which we varied different rupture model parameters, we found that the saturation is a robust feature of the ground motion that does not depend on specific kinematic rupture characteristics, except for the type of faulting. The near-fault saturation has to do with the attenuation of waves propagating along the fault and local rupture radiation pattern that also contribute to stronger ground motion variation at such distances. The simulations support the hypothesis made by several GMM authors (e.g. Graizer et al., 2011;2016), that the saturation is a consequence of the wave propagation cumulative effect being stronger at locations away from the fault where the wave generated from the energetic parts of the fault are more coherent, as opposed to short faut-distance locations along the fault.

Our ground motion simulations for thrust-type earthquakes with surface rupture suggest that the near-fault saturation for this type of rupture is weak. Moreover, for thrust faults, the strength of the horizontal motion saturation with fault distance is period dependent. These results support the hypothesis which attributes the near-fault saturation to combined radiation pattern and wave propagation effects.

Our 3D regional velocity model includes a realistic surface topography with higher elevations and roughness in the northern part of the model. The topography was extracted from the western North Carolina. Using simulated ground motions on a dense grid of stations we investigated potential topographic effects on ground motion amplitude. Overall, our analysis of topographic effects suggests that the local topography slightly amplifies (by ~30%) the ground motion amplitude in the simulated frequency range 1-3Hz.

We concluded that because of the very high Vs in the shallow layers of our regional model the surface topography, in general, has minor effects in the simulated frequency range 0-5Hz.

The capability for simulating a large set of synthetic ground motion can provide constraints on the existing GMMs, especially for large magnitudes and short distances. Scenario-based synthetics can supplement ground motion data bases for short distances and large magnitude earthquakes in the CEUS region.

In this study we used our modeling capability to simulate ground motion from the M_w7.0 1887 Charleston earthquake. Our simulation analysis favors the location of the fault and faulting mechanism proposed by Chapman and Beale (2020), and that the forward rupture directivity effects and the shallow dip angle of the buried fault might have played a significant role in the observed damage pattern.

Acknowledgements

This work was funded by the U.S. Nuclear Regulatory Commission under contract 31310021S0002, and the work of A. Pitarka, A. Rodgers, and A. Aguiar was performed under the auspices of the U.S. Department of Energy by Lawrence Livermore National Laboratory under Contract DE-AC52-07NA27344. Simulations were performed on the Quartz CPU platform and Lassen graphics processing unit accelerated platform at LLNL operated by Livermore Computing using a Computing Grand Challenge allocation.

7.0 REFERENCES

Baumann, C., and L. A. Dalguer (2014). Evaluating the compatibility of dynamic rupture-based synthetic ground motion with empirical ground-motion prediction equation, *Bull. Seismol. Soc. Am.* 104, no. 2, 634–652.

Bilham, R., and S. E. Hough (2023). The 1886 Charleston, South Carolina, earthquake: Relic railroad offset reveals rupture, *Seism. Rec.* 3, no. 4, 278–288, doi: 10.1785/0320230022.

Chapman, M. C., and R. W. Godbee (2012). Modeling geometrical spreading and the relative amplitudes of vertical and horizontal high- frequency ground motions in eastern North America, *Bull. Seismol. Soc. Am*. 102, no. 5, 1957–1975.

Chapman, M. C., J. N. Beale, A. C. Hardy, and Q. Wu (2016). Modern seismicity and the fault responsible for the 1886 Charleston, South Carolina, earthquake, *Bull. Seismol. Soc. Am.* 106, 364–372, doi: 10.1785/0120150221.

Graizer, V. (2022) Geometrical spreading an apparent anelastic attenuation of response spectral accelerations, *Soil Dynamics and Earthquake Engineering*, 162, https://doi.org/10.1016/j.soildyn.2022.107463

Graizer, V., E. Kalkan (2011). Modular filter-based approach to ground motion attenuation modeling, *Seismol. Res. Lett.* 82, no. 1, 21–31.

Graizer, V., E. Kalkan (2016). Summary of the GK15 ground-motion prediction equation for horizontal PGA and 5% Damped PSA from shallow crustal continental earthquakes, *Bull. Seism. Soc. Am.*, 106, No2, 687-707, doi: 10.1785/0120150194.

Graizer, V. (2016). Ground-Motion Prediction Equations for Central and Eastern North America. *Bull. Seism. Soc. Am.*, **106**, 1600-1612.

Graizer, V. (2017). Alternative (G-16v2) Ground-Motion Prediction Equations for Central and Eastern North America. *Bull. Seism. Soc. Am.*, **107**, 869-886.

Graizer, V. (2018). GK17 Ground-Motion Prediction Equation for Horizontal PGA and 5% Damped PSA from Shallow Crustal Continental Earthquakes. *Bull. Seism. Soc. Am.*, **108**, 380-398.

Graves, R. and A. Pitarka (2016). Kinematic Ground-Motion Simulations on Rough Faults Including Effects of 3D Stochastic Velocity Perturbations, *Bulletin of the Seismological Society of America,* **106**(5), 2136–2153, doi:10.1785/0120160088.

Goulet, C. Y. Bozorgnia, G.M. Atkinson (2021). NGA-East Ground-Motion Characterization model part I: Summary of products and model development, *Earthquake Spectra*, https://doi.org/10.1177/87552930211018723.

Herrmann, R. B. (1995). Broadband seismology and small regional seismicnetworks, in Investigation of the New Madrid Seismic Zone, K. M.Shedlock and A. C. Johnston (Editors), *U.S. Geol. Surv. Profess. Pap. 1538.*

Li, Y. G., and J. E. Vidale (1996). Low-velocity fault-zone guided waves: Numerical investigations of trapping efficiency, *Bull. Seismol. Soc. Am*. 86, 371–378.

McCallen, D., N. A. Petersson, A. Rodgers, A. Pitarka, M. Miah, F. Petrone, B. Sjogreen, N. Abrahamson, H.Tang (2020), EQSIM – A Computational Framework for Fault-to-Structure Earthquake Simulations on Exascale Computers Part I: Computational Models and Workflow, *Earthquake Spectra*, https://doi.org/10.1177/8755293020970982

McCallen, D., F. Petrone, M. Miah, A. Pitarka, A. Rodgers, N. Abrahamson (2020), EQSIM – A Multidisciplinary Framework for Fault-to-Structure Earthquake Simulations on Exascale Computers Part II: Regional Simulations of Building Response, *Earthquake Spectra*, https://doi.org/10.1177/8755293020970980

Pitarka, A., and R. Mellors (2021), Using Dense Array Waveform Correlations to Build a Velocity Model with Stochastic Variability, *Bull. Seismo. Soc. Am.*,1–21, doi: 10.1785/0120200206.

Pitarka A**.,** R. Graves, K.Irikura, H. Miyake, and A. Rodgers (2017). Performance of Irikura Recipe Rupture Model Generator in Earthquake Ground Motion Simulations with Graves and Pitarka Hybrid Approach, *Pure and Applied Geophysics*, **174**(9), doi:10.1007/s00024-017-1504-3.

Pitarka, A., R. Graves, K. Irikura, K. Miyakoshi, C. Wu, H. Kawase, A. Rodgers, and D. McCallen (2022). Refinements to the Graves–Pitarka Kinematic Rupture Generator, Including a Dynamically Consistent Slip-Rate Function, Applied to the 2019 Mw7.1 Ridgecrest Earthquake. *Bull. Seism. Soc. Am*, 112, (1):287-306. https://doi.org/10.1785/0120210138

Rodgers, A.J., A. Pitarka, R. Pankajakshan, B. Sjögreen, and N.A. Petersson (2020). Regional-Scale Three-Dimensional Ground Motion Simulations of Mw7 Earthquakes on the Hayward Fault, Northern California Resolving Frequencies 0-10 Hz and Including Site Response Corrections, *Bull. Seismo. Soc. Am.*, (published online 8/11/2020), doi: 10.1785/0120200147.

Pratt, T, M. Chapman and Q. Wu (2024) Comment on "The 1886 Charleston, South Carolina, Earthquake: Relic Railroad Offset Reveals Rupture" by Roger Bilham and Susan E. Hough. *The Seismic Record* (2025) 5 (1): 11–22. https://doi.org/10.1785/0320240002

Rodgers, A., A. Pitarka, N. A. Petersson, B. Sjogreen, D. McCallen and N. Abrahamson (2019). Broadband (0-5 Hz) fully deterministic three-dimensional ground motion simulations of a magnitude 7.0 Hayward Fault earthquake: comparison with empirical ground motion models and 3D path and site effects from source normalized intensities, *Seismo. Res. Lett*., https://doi.org/10.1785/0220180261.

Rodgers, A, A. Pitarka**,** A. Petersson, B. Sjogreen, D. McCallen (2018). Broadband (0-4 Hz) Ground Motions for a Magnitude 7.0 Hayward Fault Earthquake with 3D Structure and Topography, *Geophysical Research Letters*, doi:10.1002/2017gl076505.

Saikia, C. (1994). Modified frequency-wavenumber algorithm for regional seismograms using Filon's quadrature: modelling of L_g waves in eastern North America, *Geophysical Journal International*, Volume 118, Issue 1, July 1994, Pages 142–158, https://doi.org/10.1111/j.1365-246X.1994.tb04680.x

Somerville et al. (1997). Modifications of empirical strong motion attenuation relations to include the amplitude and duration effects of rupture directivity. *Seism. Res. Lett.,* 68(1):199-222.

Spudich P., and B. Chiu (2008) Directivity in NGA Earthquake Ground Motions: Analysis Using Isochrone Theory, *Earthquake Spectra*.

Spudich, P., Bayless, J. R., Baker, J. W., Chiou, B. S. J., Rowshandel, B., Shahi, S. K., & Somerville, P. (2013). Final Report of the NGA-West2 Directivity Working Group, PEER Report 2013-09. Pacific Earthquake Engineering Research Center, University of California, Berkeley, CA. https://peer.berkeley.edu/sites/default/files/webpeer-2013-09-paul_spudich_jeffrey_r._bayless_jack_w._baker_brian_s.j._chiou_badie_rowshandel.pdf

Taylor J., M. Celebi, A. Greer, E. Jampole, A. Masroor, S. Melton, D. Norton, N. Paul, E. Wilson, and Y. Xiao (2017). *EERI Earthquake Reconnaissance Team Report:* M5.0 Cushing Oklahoma USA Earthquake on November 7, 2016.